CORA Cork Open Research Archive
Cartlann Taighde Oscailte Chorcaí

Title	Nonlinear design of a general single-translation constraint and the resulting general spherical joint
Authors	Zhu, Jiaxiang;Li, Shiyao;Hao, Guangbo
Publication date	2025-03-20
Original Citation	Zhu, J., Li, S. and Hao, G. (2025) 'Nonlinear design of a general single-translation constraint and the resulting general spherical joint', Journal of Mechanical Design, 147(10), 103301 (22pp). https://doi.org/10.1115/1.4068101
Type of publication	Article (peer-reviewed);journal-article
Link to publisher's version	10.1115/1.4068101
Rights	© 2025, ASME. The definitive, peer reviewed and edited version of this article is available at: https://doi.org/10.1115/1.4068101 - https://creativecommons.org/licenses/by/4.0/
Download date	2026-08-07 00:58:56
Item downloaded from	https://hdl.handle.net/10468/17862

UCC
University College Cork, Ireland
Coláiste na hOllscoile Corcaigh

Nonlinear design of a general single-translation constraint and the resulting general spherical joint

Jiaxiang Zhu, Shiyao Li, Guangbo Hao*

School of Engineering and Architecture-Electrical and Electronic Engineering, University College Cork, Cork, Ireland

*Corresponding author: G.Hao@ucc.ie

Abstract

Compliant mechanisms, such as compliant spherical parallel joints, play a vital role in engineering applications, often relying on single-translation constraint wire beams. However, these wire beams have inherent shortcomings, such as manufacturing challenges and low axial stiffness. Addressing these issues is imperative and firstly leads to the nonlinear design of the General Single-Translation Constraint (GSTC) leaf beam in this paper, which offers versatility in creating diverse single-translation constraint leaf beam configurations through geometry parameter manipulation. Leveraging the GSTC leaf beam, we then designed a versatile compliant-mechanism-based general spherical joint (spherical parallel mechanism) by introducing four key parameters. The spatial kinetostatic models of the GSTC leaf beam and the general spherical joint were both formulated using a nonlinear spatial beam constraint model. Four representative specific configurations derived from the general spherical joint were further selected for FEA verification and performance comparative analysis with a focus on the centre drift. Finally, an experimental hardware was set up to test a fabricated prototype of the L-shape beam based spherical joint for the load-dependent effects and the nonlinear centre drifts. The experimental results confirm the high accuracy of the proposed nonlinear spatial models, which can facilitate model-based, rapid multi-objective optimization in future studies.

Keywords: compliant mechanism, single-translation constraint, spherical joint, general model, spatial kinetostatic model, centre drift.

1. Introduction

The wire beam provides a single-translation constraint along its axial direction (shown in Fig. 1(a)), serving as a fundamental component in the design of compliant mechanisms. From simple guiding mechanisms [1-3] to intricate compliant parallel manipulators [4-6] and spherical joints [6, 3], wire beams play a critical role. Despite their advantages in simplicity and reduced actuation, challenges arise in manufacturing when utilizing computer numerical control mills and additive manufacturing techniques. Furthermore, wire beams struggle to withstand external loads along the beam due to their low stiffness [7].

As the demand for precision flexure systems continues to rise, especially in the realm of increasingly complex flexure-based applications, addressing these challenges becomes imperative. Recognizing this need, our previous work [7] introduced a single-translation constraint I-shape leaf beam design (Fig. 1(b). Subsequently, we linearly captured the kinetostatic behavior of the I-shape leaf beam and the resulting spherical joint using the compliance matrix modeling method. Building upon this foundation, we propose an enhanced approach by introducing the GSTC leaf beam, incorporating four independent geometry parameters. This novel model facilitates the determinate synthesis of spatial force-displacement characteristics within a framework of two leaf beams based single-translation constraint. The introduction of the GSTC leaf beam marks a significant advancement, allowing for the creation of diverse single-translation constraint leaf beam designs through the manipulation of the geometry parameters. This versatility facilitates parametric optimization to enhance performance metrics such as manufacturability, spatial efficiency, and resilience to external forces.

As the fundamental component of the GSTC leaf beam is the leaf beam itself, our objective is to utilize a spatial model capable of accurately capturing its force-displacement characteristics. Several spatial modeling techniques have emerged from 2D methodologies, including the beam constraint model (BCM) [8, 9], the pseudo-rigid-body model (PRBM) [10-13], and the chained algorithm [14-16]. In particular, Sen et al. [17] introduced a spatial beam constraint model (SBCM) based on the planar BCM, which meticulously characterizes stiffness and error motions through nonlinear load-displacement relations, based on principles of virtual work. This method accurately represents nonlinear force-displacement characteristics within an intermediate translational and angular displacement range of 0.1 L and 0.1 rad, respectively. To enhance the versatility of the SBCM, this study extends its applicability to account for angular misalignments and variable cross-sections in spatial bisymmetric beams [18]. However, it's important to note that these models are exclusively applicable to beams with bisymmetric cross-sections, such as square and circular cross-sections, assuming identical moments of area for the cross-sections.

Several 3D-pseud rigid body models (PRBM) have been developed based on the planar PRBM. In ref. [19], this model provides deflection limits dependent on the beam's aspect ratio and has the potential to aid in designing spatial compliant mechanisms and analyzing planar mechanisms with large out-of-plane motions. Reference [20] introduces a chain algorithm element constructed from pseudo-rigid-body segments, enabling accurate prediction of the force-deflection relationship for beams undergoing large 3-D deflections, specifically lateral torsional buckling. However, both aforementioned models are only able to model the beam subject to end-force loads and yield relatively large errors for arbitrary loads. Reference [21] presents an enhanced version of the 3D-PRBM, specifically tailored for straight cantilever beams with rectangular cross-sections and spatial motion under arbitrary loads. Nonetheless, this model is predicated on the assumption of no moment at the free end, imposing certain limitations, particularly in structures subjected to complex loading conditions.

Nijenhuis et al. [22] introduced an analytical model using a discretized version of a finite strain spatial flexure strip formulation to derive parametric expressions describing deformation and stiffness properties. However, this model is not a closed-form solution, making interpretation challenging. To address this limitation, Nijenhuis et al. [23] proposed an alternative approach that provides closed-form expressions in a mixed stiffness and compliance matrix format tailored for flexure mechanism analysis. This approach accurately considers bending, shear, elongation, torsion, and warping deformation. Nonetheless, the model neglects load-stiffening behavior along the width direction due to axial force, leading to significant errors in strips subjected to large axial forces.

Based on the BCM, Bai et al. [24] initially introduced load-displacement relations as a parameterized tool for comprehending constraint behavior and designing compliant mechanisms with nonlinear kinetostatic behaviors, focusing primarily on rectangular cross-section beams. However, this model's applicability is limited to beams with small width-to-thickness ratios. In response, Bai et al. [25] subsequently devised a method to establish closed-form load-displacement relations tailored for strip flexures experiencing spatial deflections within an intermediate range. This resulting relation provides a parameterized framework for comprehending constraint behavior and crafting compliant mechanism designs with nonlinear kinetostatic behaviors. To simplify this complex modeling task, Bai et al. proposed an energy-based approach that treats the compliant mechanism as a whole entity, eliminating the need to analyze load equilibriums between adjacent elements [26]. However, the theorem requires the calculation of partial derivatives of the strain energy concerning applied loads, which can be cumbersome and computationally expensive, especially for complex systems. Hao et al. [27] introduced a nonlinear spatial model utilizing the BCM under small deflection and plane cross-section assumptions. These models are applicable only within the scope of small deflections, typically when all normalized displacements are less than 0.1 and for structures with large slenderness ratios (usually length-to-diameter ratios exceeding 10 for slender beams, disregarding shear deformation).

Existing beam formulations and models present a tradeoff between accuracy and mathematical complexity. To establish the GSTC leaf beam, we aim to employ an approach that is closed-form, accurate, easy to interpret, capable of capturing nonlinear kinetostatic behavior, and suitable for leaf beams with relatively large width-to-thickness ratios. The approach proposed in Ref. [25] aligns perfectly with our requirements, which will be used for the construction of the GSTC leaf beam.

Outlined below are the primary contributions of this paper:

1) This paper serves to address the gap in the general nonlinear modeling and design of single-translation constraint leaf beams by introducing the GSTC leaf beam. It enables the creation of diverse single-translation constraints through the manipulation of several key geometric parameters.
2) The design of a general spherical joint consisting of GSTC leaf beams is first proposed in this paper, which can be reduced to any specific design available in the literature. Its nonlinear spatial kinetostatic model is analytically developed, which can promote the model-based quick multi-objective optimization.
3) Several representative spherical joints are examined and compared, with a particular emphasis on center drift analysis.
4) Nonlinear FEA and experimental tests are investigated to thoroughly verify the designs and the developed spatial models.

2. Design and modelling of a general single-translation constraint leaf beam

The objective of this section is to design and model the GSTC leaf beam. Section 2.1 explains the design and presents the analytical derivation process for the GSTC leaf beam based on the nonlinear SBCM [25] in conjunction with the Free Body Diagram (FBD) method. In section 2.2, we focus on showcasing four representative configurations (Fig. 2) using the GSTC leaf beam. To ensure the credibility of our findings, we conducted a thorough verification process by comparing the analytical results with those obtained from the nonlinear FEA tool.

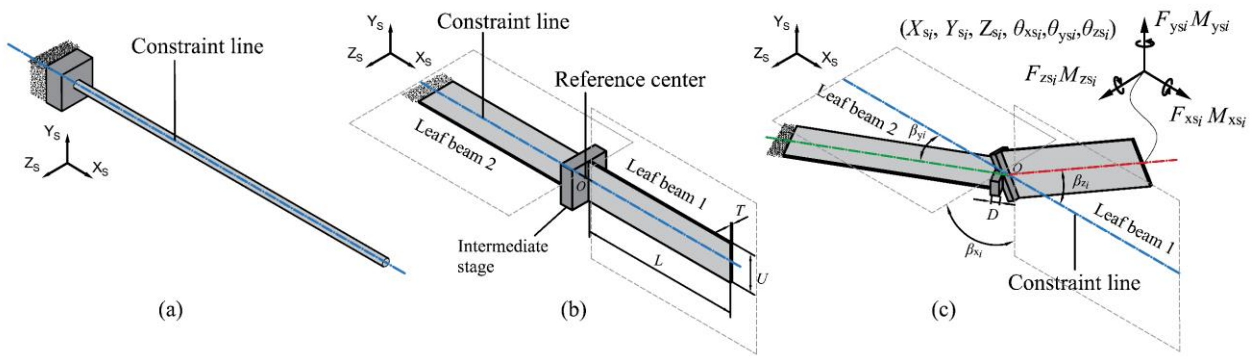

Figure 1 Compliant mechanisms with equivalent single-translation constraints: (a) wire beam with constraint line along the beam axial direction (length direction); (b) I-shape leaf beam [7]; (c) GSTC leaf beam.

2.1 The GSTC leaf beam design and model

Figure 1 illustrates several compliant mechanisms with equivalent single-translation constraints, including the GSTC leaf beam (Fig. 1(c)) that consists of two leaf beams connected in series by an intermediate stage, under the fixed global coordinate system Xs-Ys-Zs. The space configuration of the GSTC leaf beam is primarily characterized by four geometric parameters: angles β_{xi}, β_{yi}, β_{zi} and length D, as labeled in Fig. 1(c). The angle β_{xi} represents the rotation angle of leaf beam 1 about the X_S axis. The angle β_{yi} denotes the rotation angle of leaf beam 2 about the Y_S axis. The angle β_{zi} indicates the rotation angle of leaf beam 1 about the Z_S axis. The symbol D indicates the intermediate stage geometry (the length between the leaf beam 2 end and the geometry centre O).

The initial axial positions of leaf beams 1 and 2 overlap along the Xs-axis (referred to as the constraint line). Additionally, the planes in which the two leaf beams lie are initially orthogonal. These initial arrangements form the I-shape leaf beam (with parameters $\beta_{xi} = \pi/2$, $\beta_{yi} = 0$, $\beta_{zi} = 0$) as shown in Fig. 1(b). Regardless of the rotations undergone by leaf beam 1 and leaf beam 2 within plane 1 and plane 2, respectively, the single-translation constraint lines remain positioned along the intersection of these two planes (constraint space) where the leaf beams are located. By adjusting these parameters, a series of single-translation constraint leaf beam modules can be obtained. The free end of the model is subjected to a general load, encompassing combined forces and moments. The symbol i corresponds to i^{th} GSTC leaf beam.

To obtain the relationship between the tip input forces (F_{xsi}, F_{ysi}, F_{zsi}, M_{xsi}, M_{ysi}, M_{zsi},) and the tip output displacements (X_{si}, Y_{si}, Z_{si}, θ_{xsi}, θ_{ysi}, θ_{zsi},) with respect to the coordinate frame X_S-Y_S-Z_S, a sequence of rotations firstly defined by three Euler angles is employed for tip rotation. The first rotation occurs about the fixed global Y-axis by an angle of θ_{ysi}, followed by a rotation about the Z-axis by an angle of θ_{zsi}, and finally, a rotation about the X-axis by an angle of θ_{xsi}. The rotation matrix, presented below, represents an extrinsic rotation [28, 29], adhering to the right-hand rule. It is important to note that, throughout this paper, capital letters represent dimensional parameters, whereas lowercase letters denote normalized (dimensionless) parameters unless stated otherwise.

$$R_{si} = \begin{bmatrix} 1 & 0 & 0 \\ 0 & \cos(\theta_{xsi}) & -\sin(\theta_{xsi}) \\ 0 & \sin(\theta_{xsi}) & \cos(\theta_{xsi}) \end{bmatrix} \begin{bmatrix} \cos(\theta_{zsi}) & -\sin(\theta_{zsi}) & 0 \\ \sin(\theta_{zsi}) & \cos(\theta_{zsi}) & 0 \\ 0 & 0 & 1 \end{bmatrix} \begin{bmatrix} \cos(\theta_{ysi}) & 0 & \sin(\theta_{ysi}) \\ 0 & 1 & 0 \\ -\sin(\theta_{ysi}) & 0 & \cos(\theta_{ysi}) \end{bmatrix} \tag{1}$$

The kinetostatic behavior (load-displacement relationships) of the GSTC leaf beam can be obtained by proposing an analytical model, formulated using the SBCM [25] and the FBD method. The system of nonlinear equations for the analytical model can be derived based on three types of fundamental conditions: constitutive equation, force equilibrium, and geometric compatibility [30-32]. The constitutive equation (SBCM) for each leaf beam under general loading conditions is detailed in Appendix A, while the force-equilibrium equations and geometric compatibility conditions are provided in Appendix B.

A GSTC leaf beam is governed by a system of 30 equations, consisting of 12 constitutive equations, 12 force-equilibrium equations, and 6 geometric compatibility equations, which together define its spatial kinetostatic behavior. The analytical solution/model is obtained by solving this system of equations.

When incorporating the GSTC leaf beam into a complex structure, the resulting equations can be of large quantity and complex. However, the resulting computational challenge can be efficiently managed using widely available mathematical software, such as Maple, MATLAB, and Mathematica. By implementing loop functions, these tools can iteratively solve the force-displacement relationships.

2.2 FEA verification for four representative configurations

The above proposed GSTC leaf beam can be reduced to four representative configurations (Fig. 2) by assigning the parameters listed in Table 1, which are named as the I-shape leaf beam [7], the non-orthogonal leaf beam, the L-shape leaf beam (named to distinguish it from other designs such as the I-shaped and folded beams) [7], and the folded leaf beam [33-35].

The I-shape leaf beam and L-shape leaf beam were first introduced in our previous work, where they were used in the design of a compliant spherical joint. Additionally, the folded beam has been studied in various applications such as the design of spherical joints [33], XYθ motion stage [34], and bistable mechanism [35]. The non-orthogonal leaf beam, investigated for the first time in this paper, is obtained by rotating leaf beam 1 about the X_S-axis by π/2 radians (β_{xi}), about the Z_S-axis at π/6 radians (β_{zi}), and finally rotating leaf beam 2 about the Y_S-axis at π/6 radians (β_{yi}).

To validate the feasibility of the GSTC leaf beam, nonlinear FEA simulations were conducted. Each design's free end was subjected to combined forces and moments, and the resulting displacement was compared with the prediction (i.e., obtained spatial kinetostatic model of the GSTC leaf beam). The simulations were executed using the commercial software COMSOL@5.0. The material properties of the leaf beam are assigned as a commonly used material in compliant mechanisms: stainless steel, with a Poisson's ratio of 0.3 and a Young's modulus of 200 GPa. Following the assumptions of the analytical model, stages and frames were defined as rigid, and no fillets were added around sharp corners. However, caution was taken to avoid sharp corners in the connection area between the rigid part and the flexure to prevent stress singularities. Despite using a finer mesh, superior outcomes were not achieved, indicating the need for a singularity check to ensure result convergence. When constructing the 3D geometry, the intermediate stage should be carefully built to guarantee the geometry centre is located at assumed point *O*.

The rotation sequence utilized in the FEA software is not predetermined, necessitating the determination of Euler angles with a specified rotation sequence for this study. A technique outlined in Ref. [24] leverages three mutually perpendicular beams affixed to the end effector to establish a rotation matrix, which is subsequently expressed through the deformed tip coordinates of these beams, allowing for the derivation of Euler angles. Additionally, a similar approach utilizing four points is discussed in Ref. [36] also introduced a similar method based on four points. For the present study, we opt for the method outlined in Ref. [24], due to its straightforward nature.

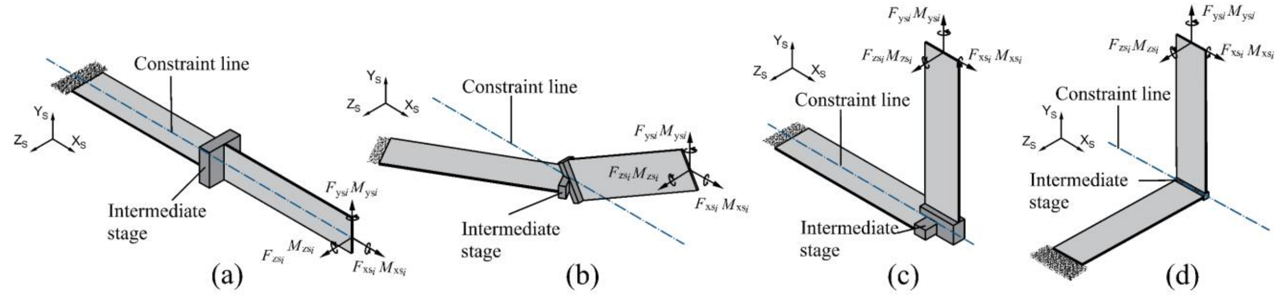

Figure 2 Four representative configurations in comparison: (a) I-shape leaf beam ($\beta_{xi} = \pi/2$; $\beta_{yi} = 0$; $\beta_{zi} = 0$); (b) non-orthogonal leaf beam ($\beta_{xi} = \pi/2$; $\beta_{yi} = \pi/6$; $\beta_{zi} = \pi/6$); (c) L-shape leaf beam ($\beta_{xi} = \pi/2$; $\beta_{yi} = 0$; $\beta_{zi} = \pi/2$); (d) folded leaf beam ($\beta_{xi} = \pi/2$; $\beta_{yi} = \pi/2$; $\beta_{zi} = \pi/2$).

Table 1 Geometry parameters of four representative configurations derived from the GSTC leaf beam

Configuration	$\boldsymbol{\beta_{xi}}$ **(rad)**	$\boldsymbol{\beta_{yi}}$ **(rad)**	$\boldsymbol{\beta_{zi}}$ **(rad)**	***D*** **(mm)**	***L*** **(mm)**	***T*** **(mm)**	***U*** **(mm)**
I-shape leaf beam	π/2	0	0	2	50	0.5	12
Non-orthogonal leaf beam	π/2	π/6	π/6	4	50	0.5	12
L-shape leaf beam	π/2	0	π/2	4	50	0.5	12
Folded leaf beam	π/2	π/2	π/2	1	50	0.5	12

Figure 3 presents the FEA verification of the non-orthogonal leaf beam with specified geometry parameters listed in Table 1. Combined forces and moments are applied to the free end of the non-orthogonal leaf beam. The resultant displacements are compared with the results captured in the FEA. The overall comparison shows a good correlation. The results show a maximum error of 8.3% which occurs at the displacement in the X-direction (X_{si}). Figure 4 illustrates a comparison of resultant displacements between FEA and analytical results, of the I-shape leaf beam. Overall, the analytical results closely correspond with the FEA outcomes. Notably, the largest deviation is observed in the resultant displacement X_{si}, with a maximum error of 6.6%. In the Y-direction, the displacement from incremental forces reaches 14 mm, exceeding 10% of the total length of the I-shape configuration, with an error of 2.8%. Figure 5 depicts the results for the L-shape configuration, wherein the displacement in the X-direction constraint attains 11 mm under combined forces and moment, showing a 3.9% error compared to analytical results. Notably, the highest error emerges in the Z-direction displacement, reaching 5.8%. Moving to Fig. 6, which displays results for the folded configuration, the largest error manifests in the rotation about the Y-axis, at approximately 6.1%.

Based on the verification conducted using the FEA tool, it can be inferred that the analytical model of the GSTC leaf beam effectively predicts the nonlinear force-displacement characteristics of GSTC leaf beams. In comparison to employing FEA tools for determining the kinetostatic characteristics of GSTC leaf beams, the analytical model of the GSTC leaf beam offers greater efficiency. This is primarily because it allows for configuration changes through simple modification of geometric parameters, thus reducing the computational time required. In the motion range spanning 10% to 20% of the GSTC leaf beam length, the maximum error remains below 10% when compared to the results obtained from FEA. Furthermore, it is noteworthy that the maximum error tends to manifest at the degree of constraint direction, which is expected, as the displacement in this direction typically remains minimal.

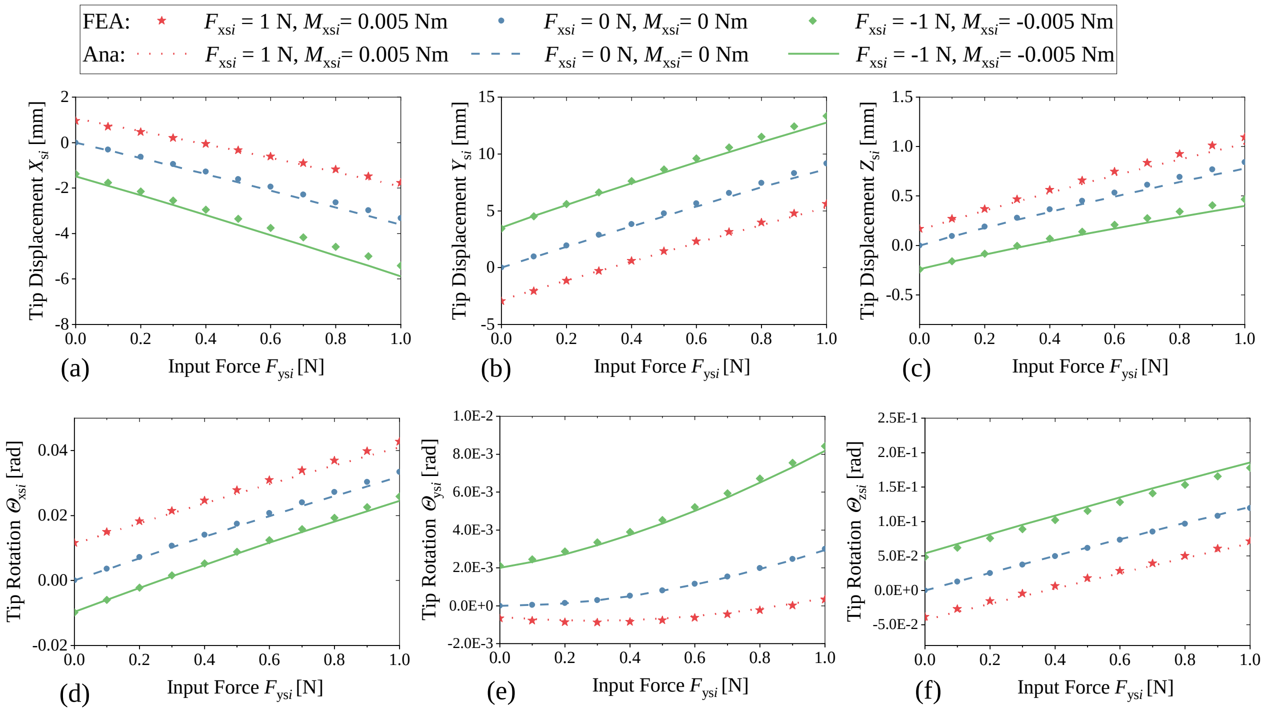

Figure 3 (Colour lines) The displacement comparison between the FEA and analytical results for the non-orthogonal leaf beam, subjected to incremental forces in the Y-direction, a constant force in the X-direction and a constant moment along the X-direction: (a) the resultant displacement X_{si} ; (b) the resultant displacement Y_{si} ; (c) the resultant displacement Z_{si} ; (d) the resultant rotation θ_{xsi} ; (e) the resultant rotation θ_{ysi} ; (f) the resultant rotation θ_{zsi} ;

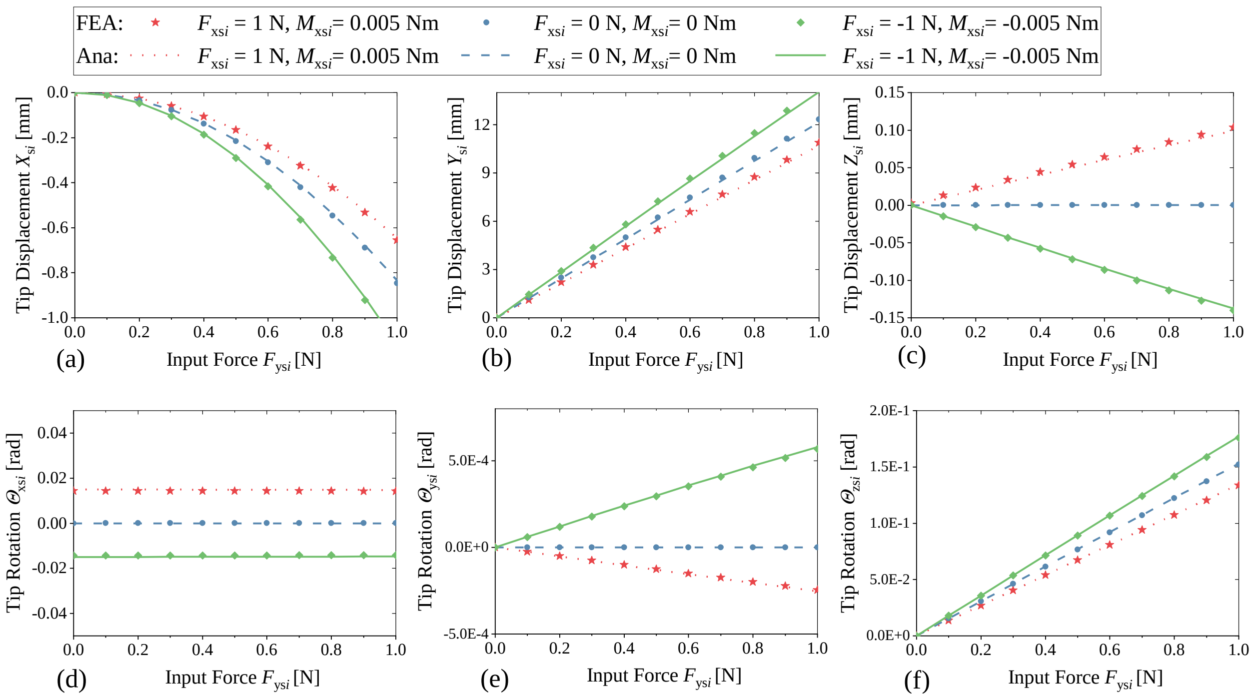

Figure 4 (Colour lines) The displacement comparison between the FEA and analytical results for the I-shape leaf beam, subjected to incremental forces in the Y-direction, a constant force in the X-direction and a constant moment along the X-direction: (a) the resultant displacement X_{si} ; (b) the resultant displacement Y_{si} ; (c) the resultant displacement Z_{si} ; (d) the resultant rotation θ_{xsi} ; (e) the resultant rotation θ_{ysi} ; (f) the resultant rotation θ_{zsi} ;

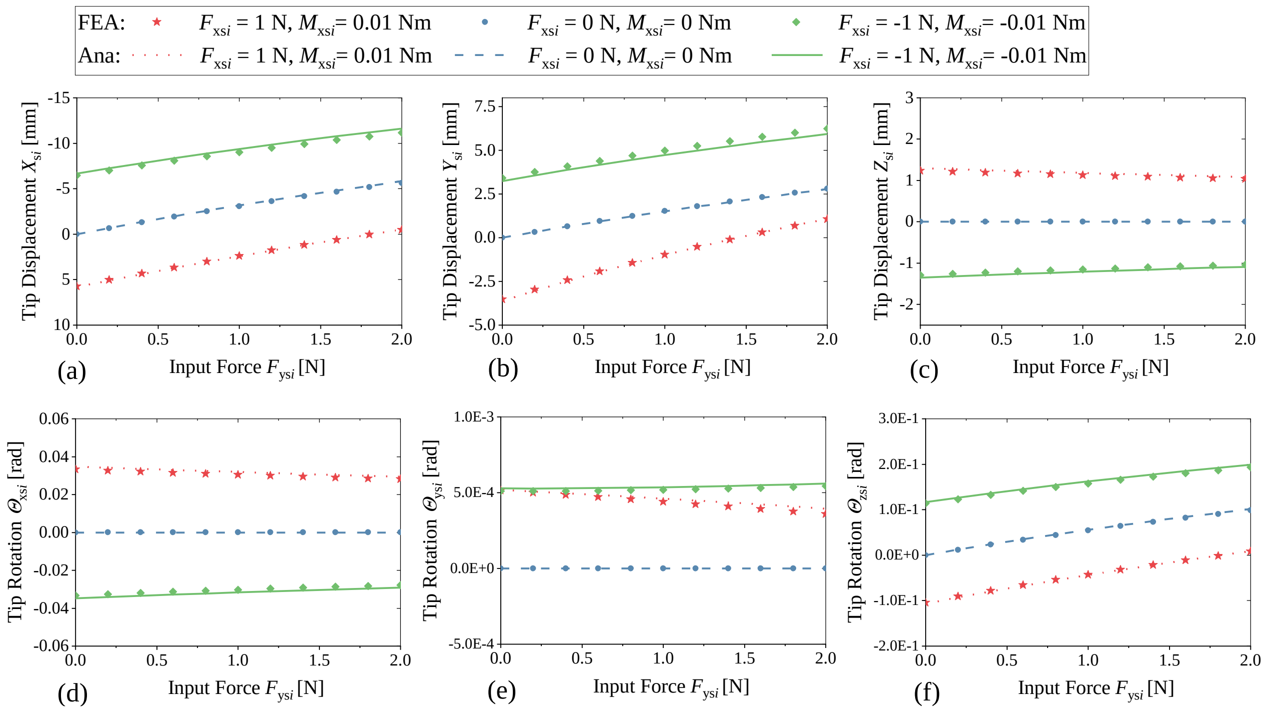

Figure 5 (Colour lines) The displacement comparison between the FEA and analytical results for the L-shape leaf beam, subjected to incremental forces in the Y-direction, a constant force in the X-direction, and a constant moment along the X-direction: (a) the resultant displacement X_{si} ; (b) the resultant displacement Y_{si} ; (c) the resultant displacement Z_{si} ; (d) the resultant rotation θ_{xsi} ; (e) the resultant rotation θ_{ysi} ; (f) the resultant rotation θ_{zsi} ;

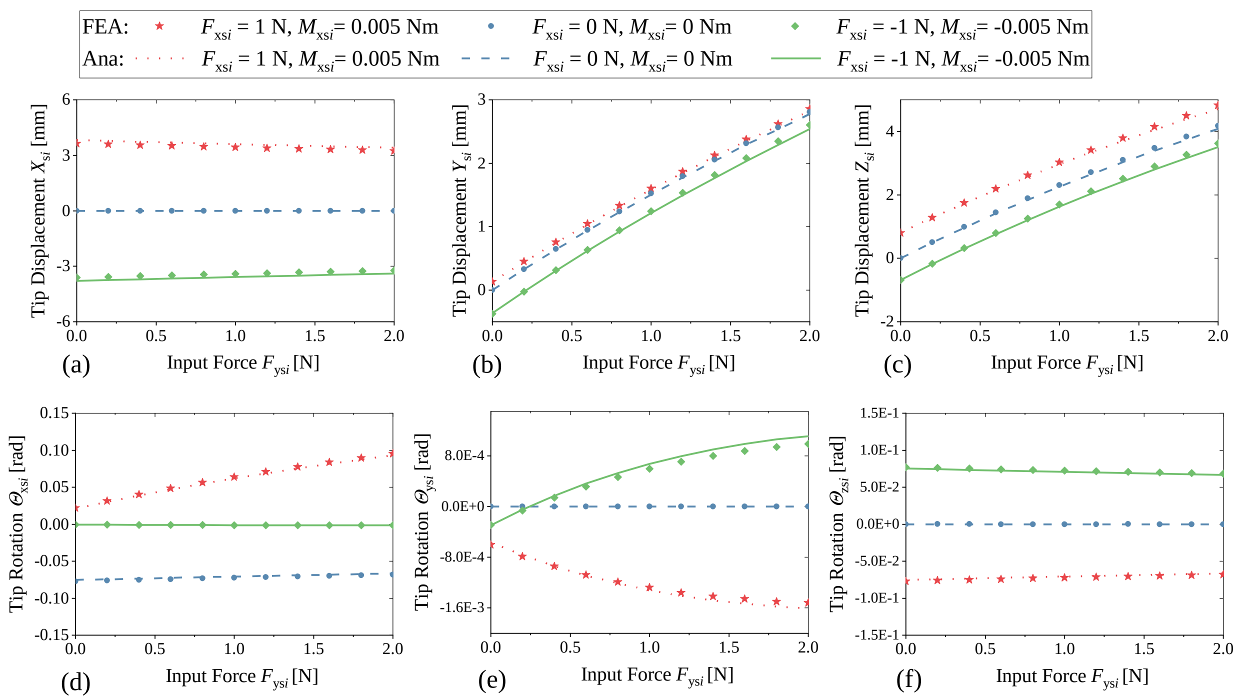

Figure 6 (Colour lines) The displacement comparison between the FEA and analytical results for the folded leaf beam, subjected to incremental forces in the Y-direction, a constant force in the X-direction and a constant moment along the X-direction: (a) the resultant displacement X_{si} ; (b) the resultant displacement Y_{si} ; (c) the resultant displacement Z_{si} ; (d) the resultant rotation θ_{xsi} ; (e) the resultant rotation θ_{ysi} ; (f) the resultant rotation θ_{zsi} ;

3. Design and nonlinear modelling of the general spherical joint

In this section, our objective is to utilize the GSTC leaf beam for the design and analysis of a general spherical joint. Initially, we will develop a general nonlinear force-displacement model for the spherical joint using the GSTC leaf beam as the basis and it will be verified by the FEA simulation. Subsequently, four representative spherical joints will then undergo centre drift analysis.

3.1 Design of a general spherical joint based on the GSTC leaf beams

A traditional compliant-mechanism-based spherical joint can be formed by the intersection of three identical single-translation constraint wire beams (lines) [37, 38] as depicted in Fig. 7(a). The joint can rotate about the remote centre (denoted as point P) in three axes. By substituting these wire beams with three identical GSTC leaf beams in terms of the positions of constraint lines, we can obtain a general spherical joint.

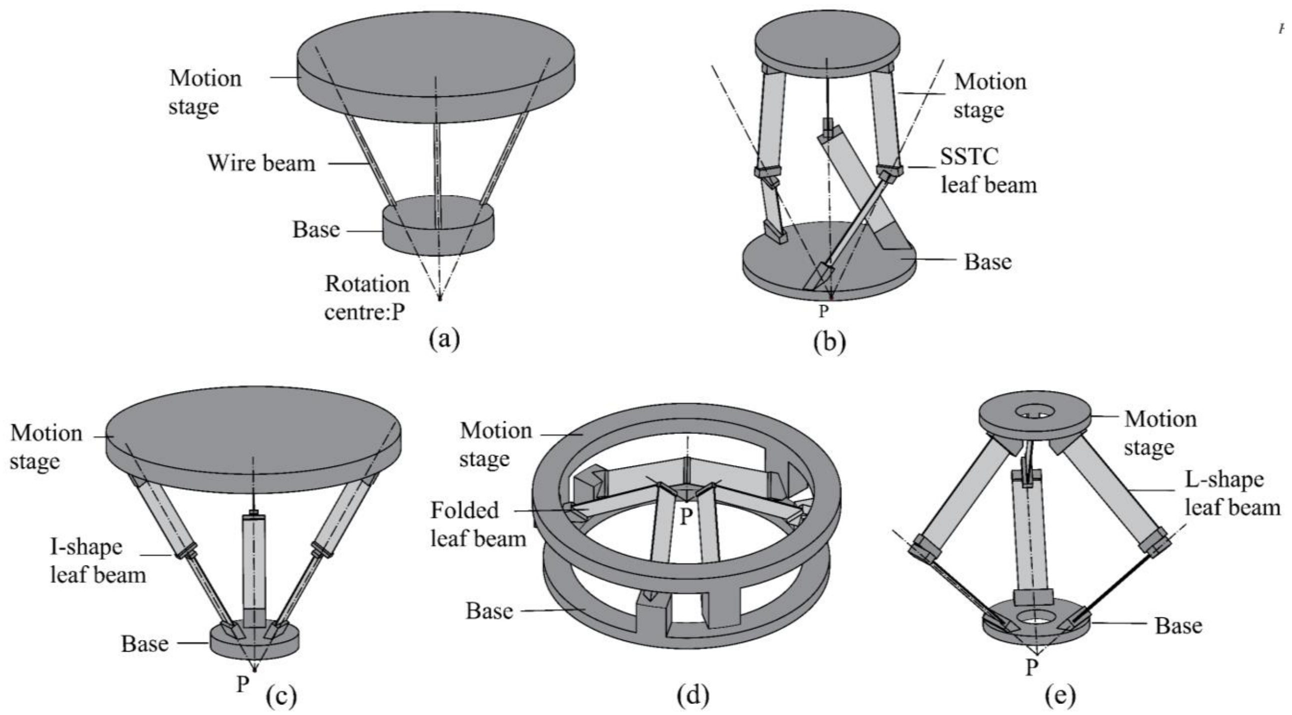

Figure 7 Spherical joints: (a) wire beam based spherical joint; (b) spherical joint using non-orthogonal leaf beams; (c) spherical joint using I-shape leaf beams; (d) spherical joint using folded leaf beams; (e) spherical joint using L-shape leaf beams. A video showcasing the design of the general spherical joint is available on YouTube: https://youtu.be/tWx_8c3q-Qw.

The general spherical joint can be reduced to several interesting designs. Figure 7(b) presents a spherical joint with non-orthogonal leaf beams (Table 1). Figure 7(c) showcases a spherical joint featuring three I-shape leaf beams, previously discussed in our work [7]. Fig. 7(d) displays a spherical joint with folded leaf beams, documented in [33, 39]. Fig. 7(e) exhibits a spherical joint with L-shape leaf beams, also introduced in our earlier research. While additional configurations are feasible using the GSTC leaf beam, this paper concentrates on analyzing these representative spherical joints, with a specific emphasis on center drift analysis, a topic less previously explored.

3.2 Nonlinear modelling of the general spherical joint

To analyse the newly designed general spherical joint, we commence by deriving the nonlinear force-displacement characteristics of the general spherical joint. This derivation parallels previous analyses, necessitating the establishment of three fundamental components: constitutive equations, force equilibrium, and geometry compatibility.

The spherical joint experiences general loading denoted as F_{xt}, F_{yt}, F_{zt}, M_{xt}, M_{yt}, and M_{zt}, at reference point O_t, resulting in spatial displacements denoted as X_t, Y_t, Z_t, θ_{xt}, θ_{yt}, and θ_{zt}, as depicted in Fig. 8(a). These displacements are defined within the global coordinate system X_T-Y_T-Z_T as shown in Fig. 8(b). Furthermore, the displacement of each GSTC leaf beam is defined in the coordinate system X_{Si}-Y_{Si}-Z_{Si} (symbol i represents the i^{th} GSTC leaf beam).

Geometry parameters γ_0, β_0, and R_0 as labeled in Fig. 8(a) and (b), are defined as the main variables for determining the orientation and position of the GSTC leaf beam. Specifically, γ_0 donates the GSTC leaf beam self-rotation about the X_S axis, β_0 donates the angle between the constraint line of the GSTC leaf beam and the center line of the spherical joint, and R_0 (non-normalized) donates the distance from the geometry center O of the GSTC leaf beam to the center line of the spherical joint. All these parameters are defined in the global X_T-Y_T-Z_T coordinate system. It is noteworthy that the orientation of the local coordinate system for each GSTC leaf beam aligns with the global X_T-Y_T-Z_T coordinate system prior to positioning. The rotation matrix, presented below, represents an extrinsic rotation adhering to the right-hand rule.

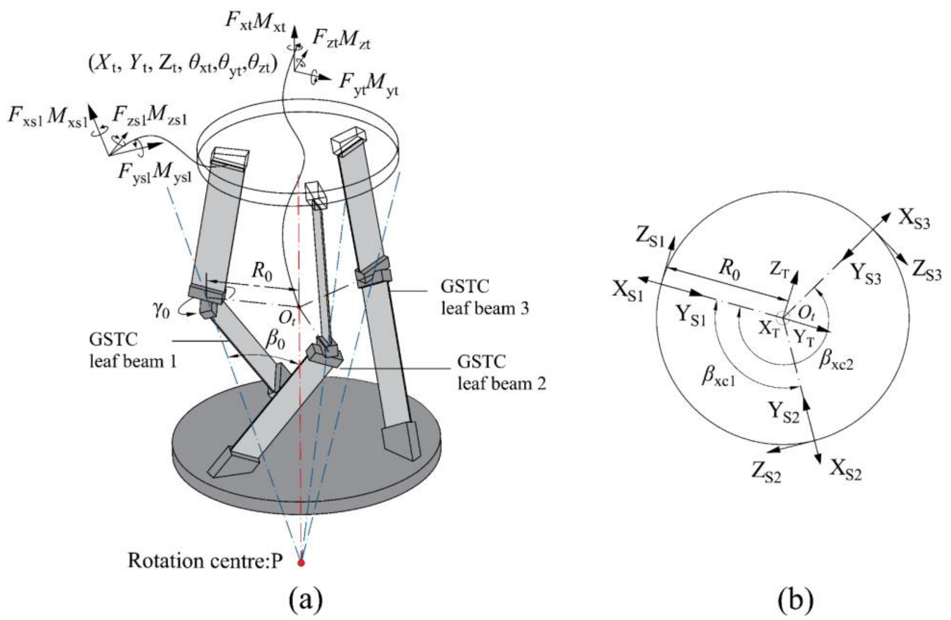

Figure 8 General spherical joint with GSTC leaf beams: (a) geometry labeling; (b) top view of the coordinate systems.

$$R_t = \begin{bmatrix} 1 & 0 & 0 \\ 0 & \cos(\theta_{xt}) & -\sin(\theta_{xt}) \\ 0 & \sin(\theta_{xt}) & \cos(\theta_{xt}) \end{bmatrix} \begin{bmatrix} \cos(\theta_{zt}) & -\sin(\theta_{zt}) & 0 \\ \sin(\theta_{zt}) & \cos(\theta_{zt}) & 0 \\ 0 & 0 & 1 \end{bmatrix} \begin{bmatrix} \cos(\theta_{yt}) & 0 & \sin(\theta_{yt}) \\ 0 & 1 & 0 \\ -\sin(\theta_{yt}) & 0 & \cos(\theta_{yt}) \end{bmatrix} \tag{2}$$

The force equilibrium of the motion stage is established based on the FBD under the deformed configuration.

$$\begin{aligned} \left[f_{xt}, f_{yt}, f_{zt}, m_{xt}, m_{yt}, m_{zt} \right]^T &= D_{T1}^T R_{ZT} R_{XT} R_{YT} R_{XS} \left[f_{xs1}, f_{ys1}, f_{zs1}, m_{xs1}, m_{ys1}, m_{zs1} \right]^T \\ &+ D_{T2}^T R_{XC1} R_{ZT} R_{XT} R_{YT} R_{XS} \left[f_{xs2}, f_{ys2}, f_{zs2}, m_{xs2}, m_{ys2}, m_{zs2} \right]^T + D_{T3}^T R_{XC2} R_{ZT} R_{XT} R_{YT} R_{XS} \left[f_{xs3}, f_{ys3}, f_{zs3}, m_{xs3}, m_{ys3}, m_{zs3} \right]^T \end{aligned} \tag{3}$$

where D_{T1}, $D_{T2,}$ and D_{T3} represent 6×6 normalized translation matrices for the free ends of GSTC leaf beams 1, 2, and 3, respectively. Their general form is provided below. In addition, the transform matrices R_{YT}, R_{XT}, and R_{ZT} donate the 6×6 rotational matrices about the Y_T, $Z_{T,}$ and X_T axis, respectively. The rotation order of the GSTC leaf beam can be defined by the user. In this work, the author adopts the order used in Solidworks for convenience in constructing the 3D model. R_{XS} is the

6×6 rotation matrix which rotates about the local coordinate X_S (intrinsic rotation). R_{XC1} and R_{XC2} donate the 6×6 rotation matrix of the GSTC leaf beam 2 and 3 respectively, about the axis X_T. The center of the moment (equilibrium position) is located at point O_t.

$$D_{Ti}=\begin{bmatrix} I_{3\times3} & \begin{matrix} 0 & d_i(3,1) & -d_i(2,1) \\ -d_i(3,1) & 0 & d_i(1,1) \\ d_i(2,1) & -d_i(1,1) & 0 \end{matrix} \\ 0_{3\times3} & I_{3\times3} \end{bmatrix} \tag{4}$$

$$d_1 = R_t(R_{zt}R_{xt}R_{yt}R_{xs}\left[\lambda_x,\ \lambda_y,\ \lambda_z\right]^T + \left[0,\ r_0,\ 0\right]^T) \tag{5}$$

$$d_2 = R_t(R_{xc1}R_{zt}R_{xt}R_{yt}R_{xs}\left[\lambda_x,\ \lambda_y,\ \lambda_z\right]^T + R_{xc1}\left[0,\ r_0,\ 0\right]^T);$$

$$d_3 = R_t(R_{xc2}R_{zt}R_{xt}R_{yt}R_{xs}\left[\lambda_x,\ \lambda_y,\ \lambda_z\right]^T + R_{xc2}\left[0,\ r_0,\ 0\right]^T);$$

$$R_{ZT}=\begin{bmatrix} R_{zt} & 0_{3\times3} \\ 0_{3\times3} & R_{zt} \end{bmatrix};\ R_{XT}=\begin{bmatrix} R_{xt} & 0_{3\times3} \\ 0_{3\times3} & R_{xt} \end{bmatrix};R_{XS}=\begin{bmatrix} R_{xs} & 0_{3\times3} \\ 0_{3\times3} & R_{xs} \end{bmatrix} \tag{6}$$

The transform matrices R_{yt}, R_{xt}, and R_{zt} donate the 3×3 rotation matrices about the Y_T, Z_T, and X_T axis, respectively, which are used to define the orientation of the free end of the GSTC leaf beam. These three rotations contribute to the angle of β_0, which is known. R_{xs} is the 3×3 rotation matrix which rotates about the local coordinate X_S (intrinsic rotation). R_{xc1} and R_{xc2} donate the 3×3 rotation matrix about the X_T-axis of the GSTC leaf beam 2 and 3 respectively, about the axis X_T. λ_x, λ_y and λ_z donate the coordinates of the free end of the GSTC leaf beam 1 relative to the X_T-Y_T-Z_T coordinate before the rotation of angle β_0. r_0 donates the normalized R_0.

$$R_{yt}=\begin{bmatrix} \cos(\beta_{yt}) & 0 & \sin(\beta_{yt}) \\ 0 & 1 & 0 \\ -\sin(\beta_{yt}) & 0 & \cos(\beta_{yt}) \end{bmatrix};R_{zt}=\begin{bmatrix} \cos(\beta_{zt}) & -\sin(\beta_{zt}) & 0 \\ \sin(\beta_{zt}) & \cos(\beta_{zt}) & 0 \\ 0 & 0 & 1 \end{bmatrix};R_{xt}=\begin{bmatrix} 1 & 0 & 0 \\ 0 & \cos(\beta_{xt}) & -\sin(\beta_{xt}) \\ 0 & \sin(\beta_{xt}) & \cos(\beta_{xt}) \end{bmatrix} \tag{7}$$

$$R_{xs}=\begin{bmatrix} 1 & 0 & 0 \\ 0 & \cos(\gamma_0) & -\sin(\gamma_0) \\ 0 & \sin(\gamma_0) & \cos(\gamma_0) \end{bmatrix};\ R_{xc1}=\begin{bmatrix} 1 & 0 & 0 \\ 0 & \cos(\beta_{xc1}) & -\sin(\beta_{xc1}) \\ 0 & \sin(\beta_{xc1}) & \cos(\beta_{xc1}) \end{bmatrix};\ R_{xc2}=\begin{bmatrix} 1 & 0 & 0 \\ 0 & \cos(\beta_{xc2}) & -\sin(\beta_{xc2}) \\ 0 & \sin(\beta_{xc2}) & \cos(\beta_{xc2}) \end{bmatrix} \tag{8}$$

The geometric compatibility between the free end of each GSTC leaf beam and the motion stage can be derived as follows. It is important to note that the initial position of the force and displacement relationship of the motion stage is represented at the position of point O_{t}.

$$R_{\mathrm{zt}}R_{\mathrm{xt}}R_{\mathrm{yt}}R_{\mathrm{sx}}\left[x_{\mathrm{s1}},\ \mathrm{y}_{\mathrm{s1}},\ \mathrm{z}_{\mathrm{s1}}\right]^{\mathrm{T}}=(R_{\mathrm{t}}-I_{3\times3})(R_{\mathrm{zt}}R_{\mathrm{xt}}R_{\mathrm{yt}}R_{\mathrm{sx}}\left[\lambda_{\mathrm{x}},\ \lambda_{y},\ \lambda_{z}\right]^{\mathrm{T}}+\left[0,\ r_{0},\ 0\right]^{\mathrm{T}})+\left[x_{\mathrm{t}},\ y_{\mathrm{t}},\ z_{\mathrm{t}}\right]^{\mathrm{T}} \tag{9}$$

$$R_{\mathrm{zt}}R_{\mathrm{xt}}R_{\mathrm{yt}}R_{\mathrm{sx}}\left[\theta_{\mathrm{xs1}},\ \theta_{\mathrm{ys1}},\ \theta_{\mathrm{zs1}}\right]^{\mathrm{T}}=\left[\theta_{\mathrm{xt}},\ \theta_{\mathrm{yt}},\ \theta_{\mathrm{zt}}\right]^{\mathrm{T}};$$

$$R_{\mathrm{xc1}}R_{\mathrm{zt}}R_{\mathrm{xt}}R_{\mathrm{yt}}R_{\mathrm{sx}}\left[x_{\mathrm{s2}},\ \mathrm{y}_{\mathrm{s2}},\ \mathrm{z}_{\mathrm{s2}}\right]^{\mathrm{T}}=(R_{\mathrm{t}}-I_{3\times3})(R_{\mathrm{xc1}}R_{\mathrm{zt}}R_{\mathrm{xt}}R_{\mathrm{yt}}R_{\mathrm{sx}}\left[\lambda_{\mathrm{x}},\ \lambda_{y},\ \lambda_{z}\right]^{\mathrm{T}}+R_{\mathrm{xc1}}\left[0,\ r_{0},\ 0\right]^{\mathrm{T}})+\left[x_{\mathrm{t}},\ y_{\mathrm{t}},\ z_{\mathrm{t}}\right]^{\mathrm{T}} \tag{10}$$

$$R_{\mathrm{xc1}}R_{\mathrm{z}}R_{\mathrm{x}}R_{\mathrm{y}}R_{\mathrm{sx}}\left[\theta_{\mathrm{xs2}},\ \theta_{\mathrm{ys2}},\ \theta_{\mathrm{zs2}}\right]^{\mathrm{T}}=\left[\theta_{\mathrm{xt}},\ \theta_{\mathrm{yt}},\ \theta_{\mathrm{zt}}\right]^{\mathrm{T}};$$

$$R_{\mathrm{xc2}}R_{\mathrm{zt}}R_{\mathrm{xt}}R_{\mathrm{yt}}R_{\mathrm{sx}}\left[x_{\mathrm{s3}},\ \mathrm{y}_{\mathrm{s3}},\ \mathrm{z}_{\mathrm{s3}}\right]^{\mathrm{T}}=(R_{\mathrm{t}}-I_{3\times3})(R_{\mathrm{xc2}}R_{\mathrm{zt}}R_{\mathrm{xt}}R_{\mathrm{yt}}R_{\mathrm{sx}}\left[\lambda_{\mathrm{x}},\ \lambda_{y},\ \lambda_{z}\right]^{\mathrm{T}}+R_{\mathrm{xc2}}\left[0,\ r_{0},\ 0\right]^{\mathrm{T}})+\left[x_{\mathrm{t}},\ y_{\mathrm{t}},\ z_{\mathrm{t}}\right]^{\mathrm{T}} \tag{11}$$

$$R_{\mathrm{xc2}}R_{\mathrm{zt}}R_{\mathrm{xt}}R_{\mathrm{yt}}R_{\mathrm{sx}}\left[\theta_{\mathrm{xs3}},\ \theta_{\mathrm{ys3}},\ \theta_{\mathrm{zs3}}\right]^{\mathrm{T}}=\left[\theta_{\mathrm{xt}},\ \theta_{\mathrm{yt}},\ \theta_{\mathrm{zt}}\right]^{\mathrm{T}};$$

In total, there are 114 equations, which include 3×30 force-displacement relations of the GSTC leaf beams, 6 force-equilibrium equations, and 18 geometry compatibility equations. The system of nonlinear equations was solved by MATLAB using solver *fsolve*. The feasibility of this general spherical joint model is verified by the FEA simulation using *Comsol*. A combined force and moment is applied to the motion stage at point O_{t}. The displacement results are compared with the results obtained in *Comsol*.

4. FEA verification of the general spherical joint

This section focuses on the FEA verification of the general force-displacement model of the general spherical joint. Section 4.1 illustrates the verification of the force-displacement relationship of the motion stage at reference point O_{t}. Section 4.2 demonstrates the verification of the resultant centre drift under combined forces and moments.

4.1 Force-displacement relationship of the motion stage

The developed general force-displacement model for spherical joints was verified using nonlinear FEA simulations. Four representative spherical joints, described in Section 3.1, were configured with the same initial geometry parameters $\gamma_0 = 0$, $\beta_0 = \pi/4$, and $R_0 = 50$ mm, and the rest parameters are defined in Table 1. The material properties of the leaf beam are set up as the same as those in Sec. 2.2. The other parts are assumed to be rigid. The deformed shape in FEA of each spherical joint under combined forces and moments is shown in Appendix C.

Figure 9 shows the comparison results between the analytical model and the FEA simulation for the spherical joint with non-orthogonal leaf beams subjected to combined forces and moments. The resultant displacements show good agreement, where the maximum error is 9.1% while the rotation along the Y-axis reaches about 0.12 radians. Figure 10 presents a comparison between analytical and FEA results for the spherical joint featuring I-shape leaf beams. The largest deviation, at 11.8%, occurs in the X-direction tip displacement of the motion stage. However, displacements in other directions exhibit a closer alignment with FEA results, with a maximum error of 6.5%. In Fig. 11, comparing the spherical joint with L-shape leaf beams, overall agreement between analytical and FEA results is evident. Yet, similar to Fig. 10, the greatest deviation, 9.2%, is observed in the X-direction displacement. Fig. 12 extends this comparison to spherical joints with folded leaf beams, showing a similar pattern of agreement to the FEA results. However, the X-direction displacement (X_t) exhibits a 9.8% difference under a 0.085 radians rotation along the Y-direction. This disparity is reasonable as X_t, constrained by design, consistently remains small.

While the developed GSTC leaf beam effectively captures force-displacement characteristics, it shows a relatively larger error in predicting constrained displacement compared to degrees of freedom. This discrepancy is understandable given the inherently minor displacements in constrained degrees, aligning with expectations.

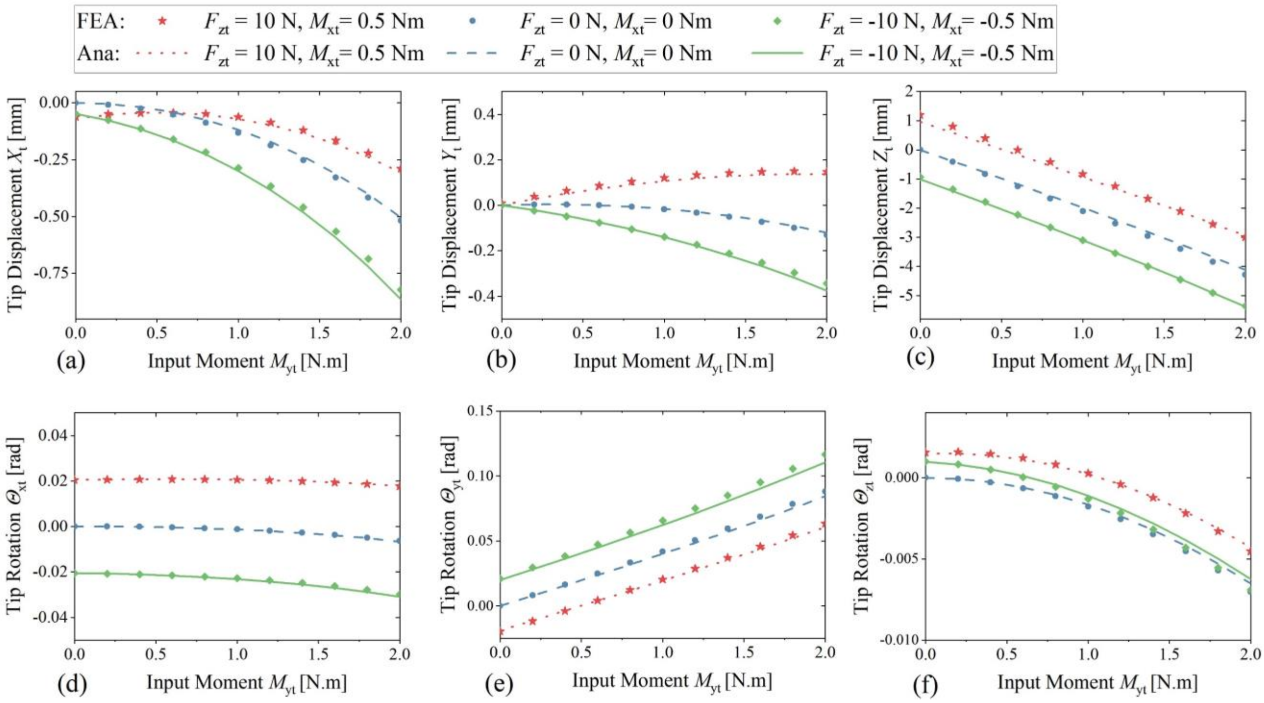

Figure 9 (Colour lines) The displacement comparison between the FEA and analytical results for the spherical joint with non-orthogonal leaf beams, subjected to incremental moment along the Y-direction, a constant moment along the X-direction and a constant force in the Z-direction: (a) the resultant displacement X_t; (b) the resultant displacement Y_t; (c) the resultant displacement Z_t; (d) the resultant rotation θ_{xt}; (e) the resultant rotation θ_{yt}; (f) the resultant rotation θ_{zt};

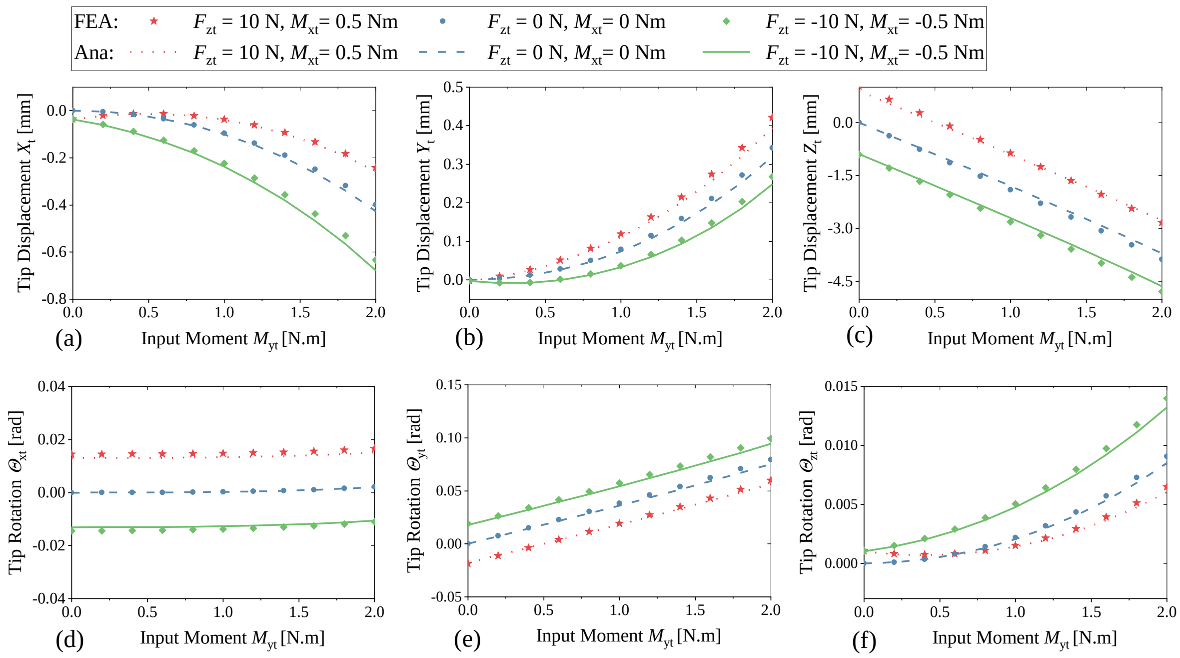

Figure 10 (Colour lines) The displacement comparison between the FEA and analytical results for the spherical joint with I-shape leaf beams, subjected to incremental moment along the Y-direction, a constant moment along the X-direction and a constant force in the X-direction: (a) the resultant displacement X_t; (b) the resultant displacement Y_t; (c) the resultant displacement Z_t; (d) the resultant rotation θ_{xt}; (e) the resultant rotation θ_{yt}; (f) the resultant rotation θ_{zt};

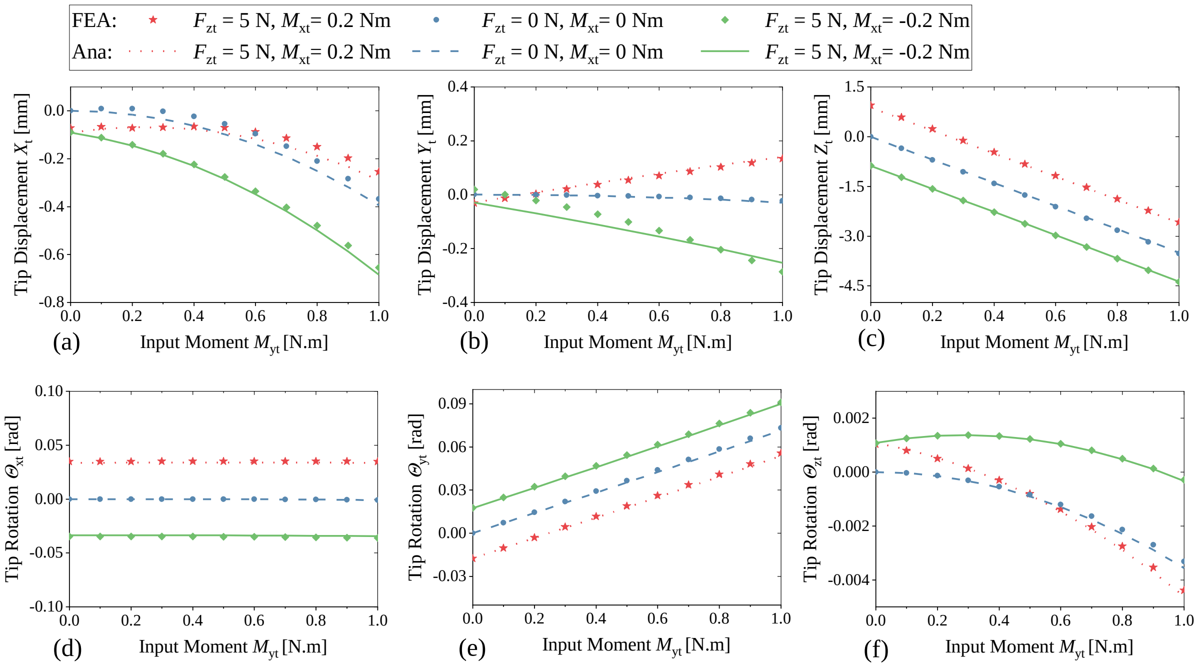

Figure 11 (Colour lines) The displacement comparison between the FEA and analytical results for the spherical joint with L-shape leaf beams, subjected to incremental moment along the Y-direction, a constant moment along the X-direction and a constant force in the X-direction: (a) the resultant displacement X_t; (b) the resultant displacement Y_t; (c) the resultant displacement Z_t; (d) the resultant rotation θ_{xt}; (e) the resultant rotation θ_{yt}; (f) the resultant rotation θ_{zt};

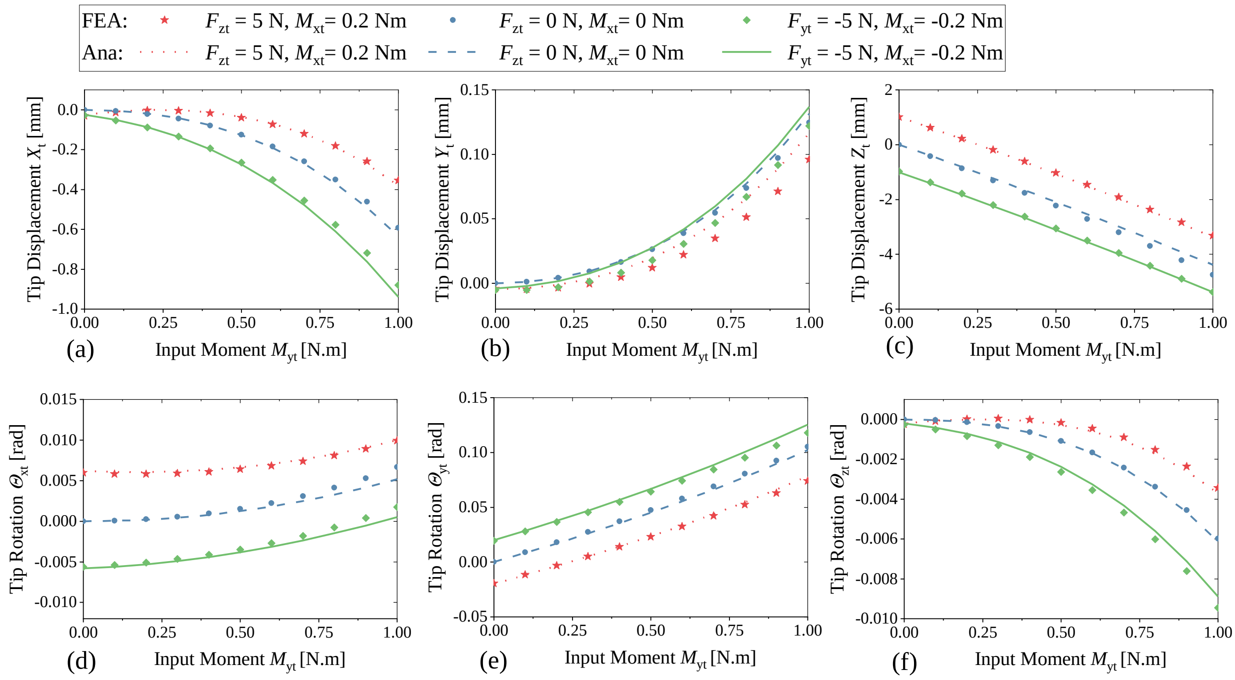

Figure 12 (Colour lines) The displacement comparison between the FEA and analytical results for the spherical joint with folded leaf beams, subjected to incremental moment along the Y-direction, a constant moment along the X-direction and a constant force in the X-direction: (a) the resultant displacement X_t; (b) the resultant displacement Y_t; (c) the resultant displacement Z_t; (d) the resultant rotation θ_{xt}; (e) the resultant rotation θ_{yt}; (f) the resultant rotation θ_{zt};

4.2 Center drift verification

Centre drift, in this context, refers to any deviation from the intended rotation centre of the joint. Investigating this drift is crucial for optimizing system performance and ensuring that movements are accurate and precise. In many applications, precision and accuracy are paramount for safety. Significant centre drift in a spherical joint can result in errors in positioning or movement. Here, d_{xc}, d_{yc} and d_{zc} are used to represent the normalised centre drift in the X, Y, and Z direction, respectively, in the global coordinate X_T-Y_T-Z_T. the centre drift can be derived as below.

$$\begin{bmatrix} d_{xc} \\ d_{yc} \\ d_{zc} \end{bmatrix} = \begin{bmatrix} x_t \\ y_t \\ z_t \end{bmatrix} + (R_t - I_{3\times3}) \begin{bmatrix} \dfrac{r_0}{\tan\beta_0} \\ 0 \\ 0 \end{bmatrix} \tag{12}$$

To verify the accuracy of the general analytical model for predicting centre drift in spherical joints, FEA simulations were conducted. Combined forces and moments were applied to the spherical joint, and the resultant centre drifts in the X, Y, and Z directions were captured and compared.

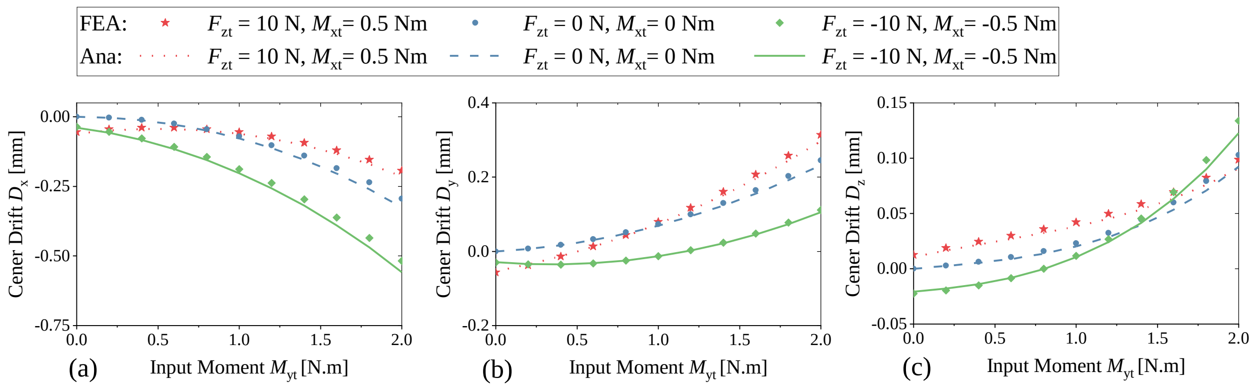

Figure 13 (Colour lines) The centre drift comparison between the FEA and analytical results for the spherical joint with non-orthogonal leaf beams, subjected to incremental moment along the Y-direction, a constant moment along the X-direction and a constant force in the X-direction: (a) the resultant displacement D_{xc}; (b) the resultant displacement D_{yc}; (c) the resultant displacement D_{zc};

Figure 13 presents the FEA verification of the spherical joint with non-orthogonal leaf beams, revealing a maximum error of approximately 8.5% between the analytical model and FEA at the centre drift in the Z-direction. The observed maximum centre drift reaches 0.56 mm in the X-direction. Similarly, Figure 14 displays the verification for the spherical joint with I-shape leaf beams, where similar nonlinear patterns are evident. The comparison between analytical and FEA results shows a good correlation, with a maximum error of 7.1%. Figures 15 and 16 illustrate the comparison results for spherical joints with L-shape and folded leaf beams, respectively. The error between analytical and FEA results is 9.3% for the L-shape leaf beams and 7.5% for the folded leaf beams.

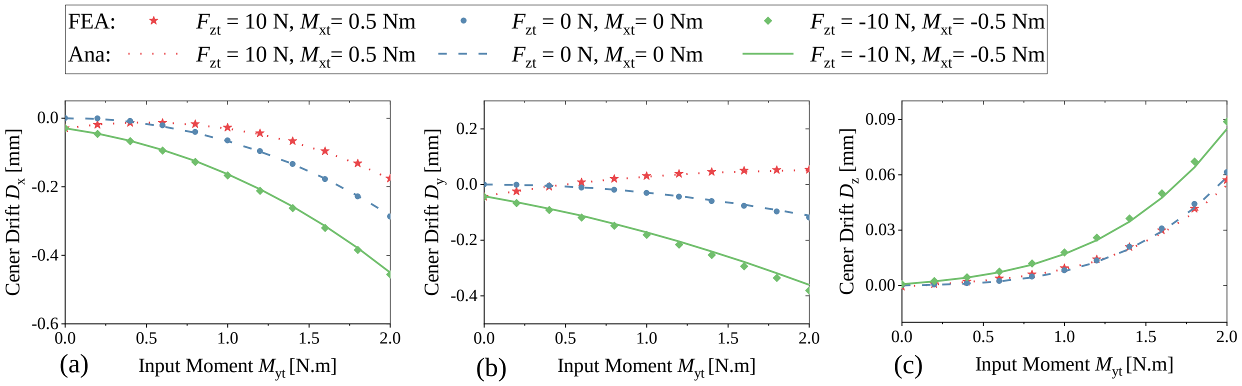

Figure 14 (Colour lines) The centre drift comparison between the FEA and analytical results for the spherical joint with I-shape leaf beams, subjected to incremental moment along the Y-direction, a constant moment along the X-direction and a constant force in the X-direction: (a) the resultant displacement D_{xc}; (b) the resultant displacement D_{yc}; (c) the resultant displacement D_{zc};

Overall, the FEA verification of the centre drift demonstrates a good correlation with the analytical results, with errors consistently below 10% across all four types of spherical joints. The motion stage rotation in the Y-axis reaches approximately 0.1 radians, subjected to combined forces and moments.

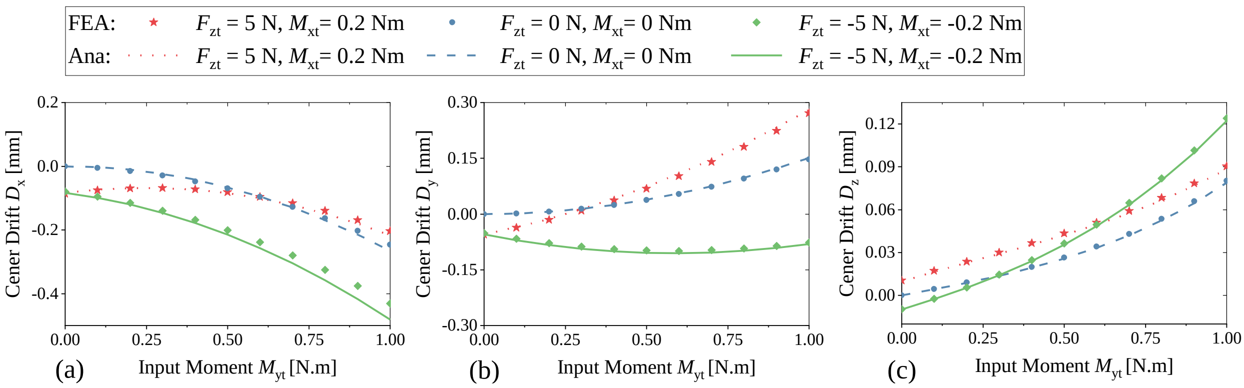

Figure 15 (Colour lines) The centre drift comparison between the FEA and analytical results for the spherical joint with L-shape leaf beams, subjected to incremental moment along the Y-direction, a constant moment along the X-direction and a constant force in the X-direction: (a) the resultant displacement D_{xc}; (b) the resultant displacement D_{yc}; (c) the resultant displacement D_{zc};

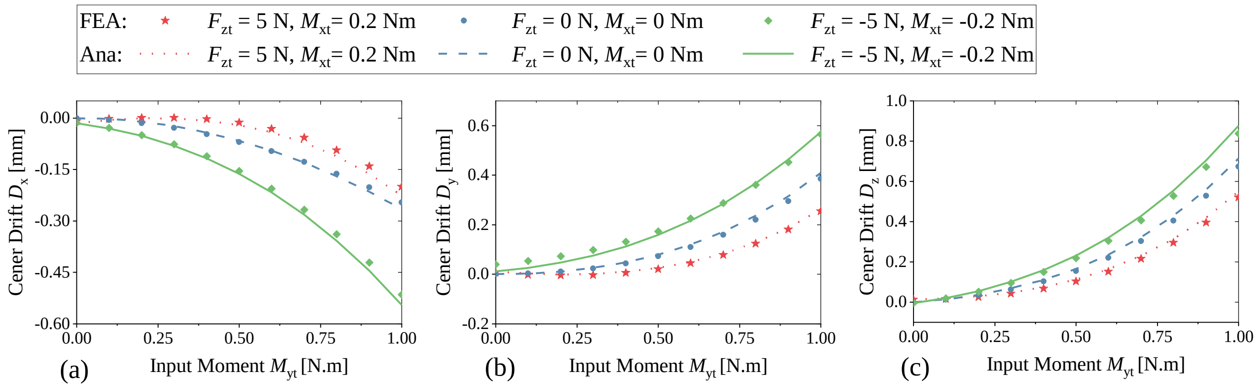

Figure 16 (Colour lines) The centre drift comparison between the FEA and analytical results for the spherical joint with folded leaf beams, subjected to incremental moment along the Y-direction, a constant moment along the X-direction and a constant force in the X-direction: (a) the resultant displacement $D_{xc;}$ (b) the resultant displacement D_{yc}; (c) the resultant displacement D_{zc}.

5. Centre drift analysis of several specific spherical joints

This section focuses on the centre drift analysis of four representative spherical joints. To provide a comprehensive analysis, the geometric parameters γ_0, β_0, and R_0, which determine the spatial position and orientation of the GSTC leaf beam, will be considered to understand their impact on the centre drift of the spherical joints. Four representative spherical joints, described in Section 3.1, were configured with the initial geometry parameters $\gamma_0 = 0$, $\beta_0 = \pi/4$, and $R_0 = 50$ mm. The remaining parameters are defined in Table 1, except for the length of the intermediate stage D, which is consistently set to 2 mm across all spherical joints.

Figure 17 presents the centre drift analysis of spherical joints equipped with non-orthogonal leaf beams, subjected to constant rotations ($\theta_{xt} = 0.2$ rad, $\theta_{yt} = 0.3$ rad and $\theta_{zt} = 0.5$ rad). As depicted in figures (a), (b), and (c), it is evident that a larger value of β_0 (ranging from $\pi/6$ to $\pi/3$) generally results in reduced centre drift. Conversely, figures (d), (e), and (f) illustrate that a larger value of R_0 (ranging from 40 mm to 60 mm) correlates with increased centre drift. Overall, the value of the centre drift in all directions fluctuates between 0 mm to 0.71 mm.

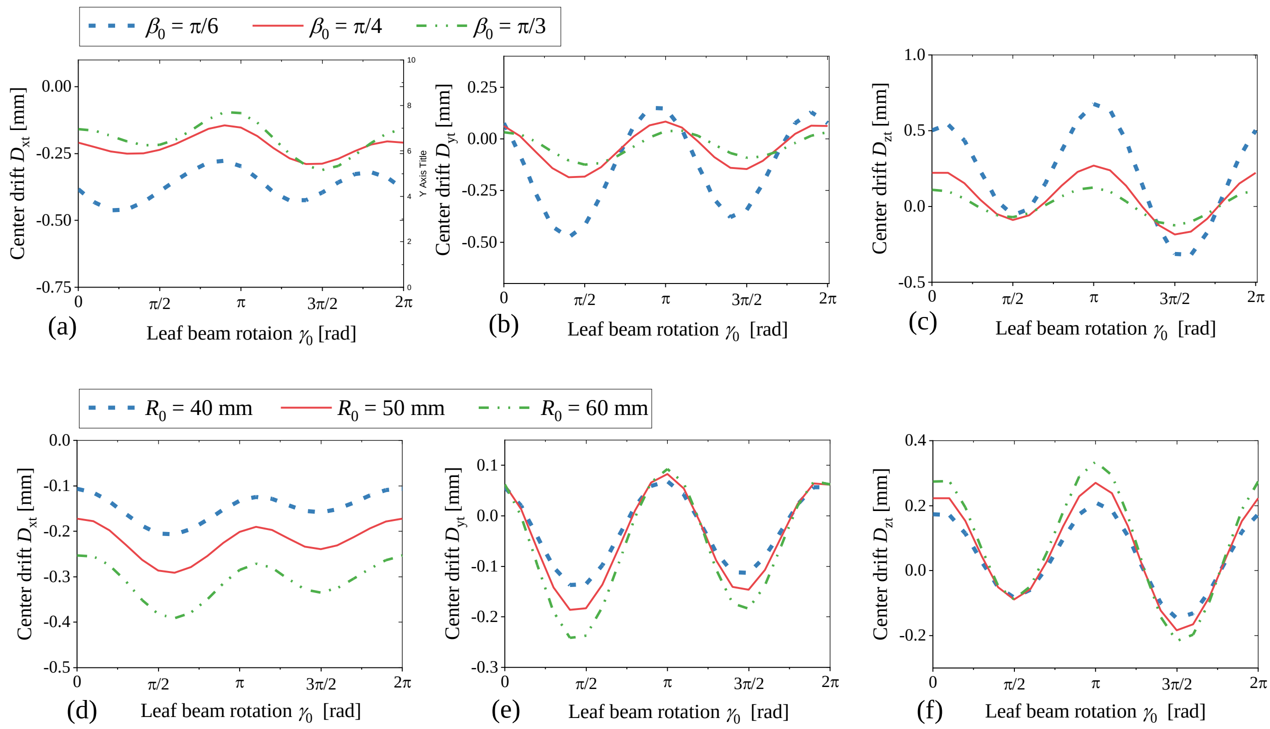

Figure 17 (Colour lines) The influence of geometry parameters γ_0, β_0, and R_0 on the center drift of the spherical joint with non-orthogonal leaf beams under constant motion stage rotation (θ_{xt} = 0.2 rad, θ_{yt} = 0.3 rad and θ_{zt} = 0.5 rad): (a), (b), and (c) illustrate the incremental changes in γ_0 and β_0 with a constant R_0 value of 50 mm; (d), (e), and (f) showcase the incremental changes in γ_0 and R_0 with a constant β_0 value of π/4;

Figure 18 illustrates the centre drift analysis of the spherical joint with I-shape leaf beams. It is evident from Figs. 18(a), (b), and (c) that a larger value of β_0 (ranging from π/6 to π/3) generally produces smaller centre drift, with the peaks of the centre drift shifting as β_0 changes. Figs. 18(d), (e), and (f) indicate that an increase in the value of R_0 corresponds to a larger centre drift. Overall, the value of the centre drift in all directions fluctuates between 0 mm to 0.55 mm.

A similar analysis is conducted for a spherical joint employing L-shape leaf beams, as demonstrated in Fig.19. It becomes apparent from Figs. 19(a), (b), and (c) that, for the same range of rotation, a larger value of β_0 results in a diminished centre drift across all directions. Conversely, Fig. 19(d), (e), and (f) indicate that an increase in the length of R_0 genuinely corresponds to a larger centre drift. Overall, the value of the centre drift in all directions fluctuates between 0 mm to 0.61 mm.

The centre drift for the spherical joint employing folded leaf beams is presented in Fig. 20. Overall, it is evident that a lower value of β_0 leads to a higher centre drift in all directions. Figs. 20(d), (e), and (f) further indicate that an increase in R_0 corresponds to a larger centre drift. Overall, the value of the centre drift in all directions fluctuates between 0 mm to 0.78 mm.

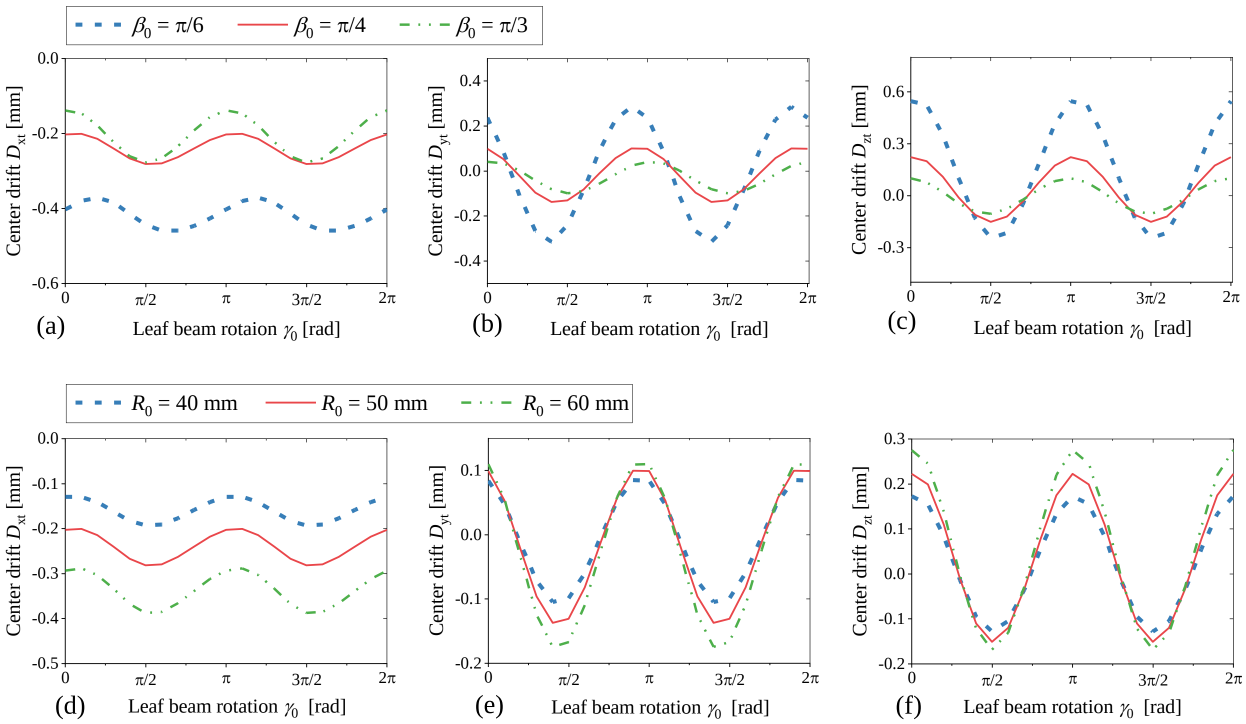

Figure 18 (Colour lines) The influence of geometry parameters γ_0, β_0, and R_0 on the center drift of the spherical joint with I-shape leaf beams under constant motion stage rotation (θ_{xt} = 0.2 rad, θ_{yt} = 0.3 rad and θ_{zt} = 0.5 rad): (a), (b), and (c) illustrate the incremental changes in γ_0 and β_0 with a constant R_0 value of 50 mm; (d), (e), and (f) showcase the incremental changes in γ_0 and R_0 with a constant β_0 value of π/4;

Determining the exact value of γ_0 for the spherical joint with optimal performance, characterized by minimal centre drift in all directions, poses a challenge due to potential variations in the smallest centre drift across different directions. For instance, in Fig. 18, the designs with γ_0 = 1.1π radians and 0π radians have the lowest value of centre drift in the X-direction. For the Y-direction, the designs with γ_0 = 0.7π and 1.7π radians have the lowest value of centre drift. The designs with γ_0 = 0.3π and 1.3π radians have the lowest value of centre drift in the Z-direction. Moreover, the activation of the spherical joint, involving different combinations of input further influences the γ_0 value associated with the smallest centre drift. However, Table 2 provides a comparison of the maximum centre drift in each direction for the four spherical joints, offering insights into which design has the best performance.

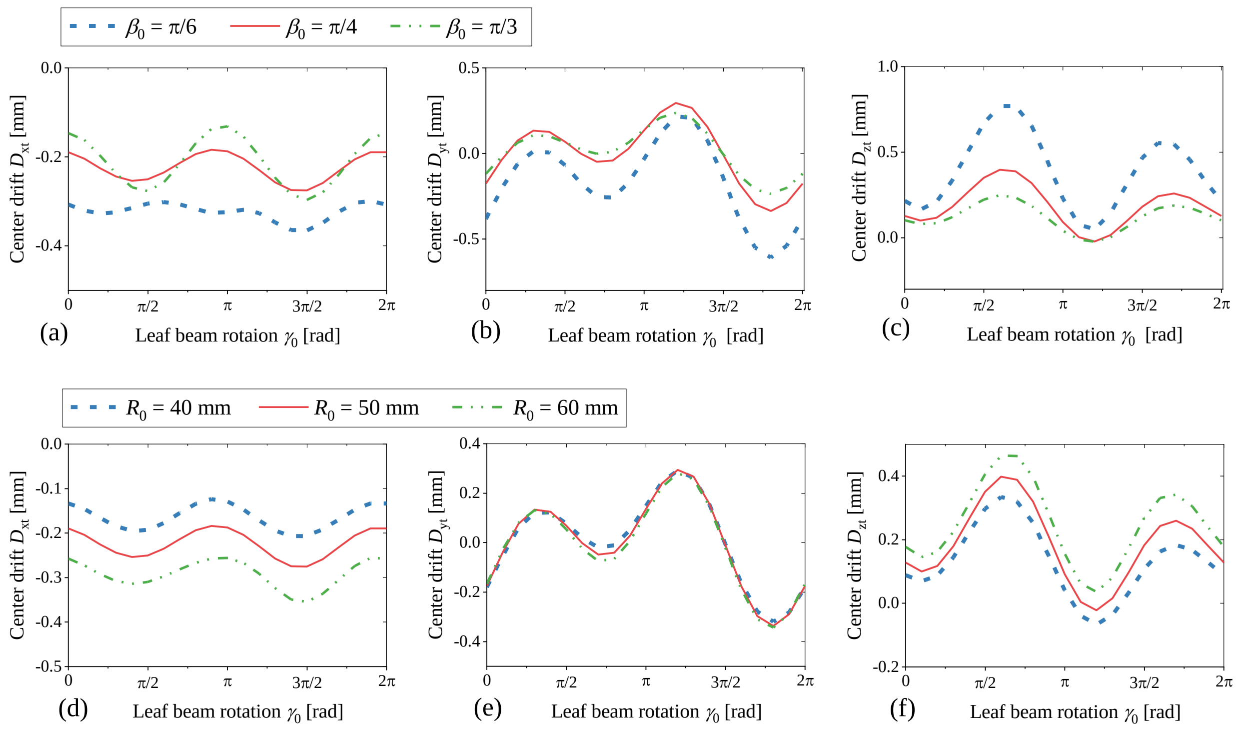

Figure 19 (Colour lines) The influence of geometry parameters γ_0, β_0, and R_0 on the center drift of the spherical joint with L-shape leaf beams under constant motion stage rotation (θ_{xt} = 0.2 rad, θ_{yt} = 0.3 rad and θ_{zt} = 0.5 rad): (a), (b), and (c) illustrate the incremental changes in γ_0 and β_0 with a constant R_0 value of 50 mm; (d), (e), and (f) showcase the incremental changes in γ_0 and R_0 with a constant β_0 value of π/4;

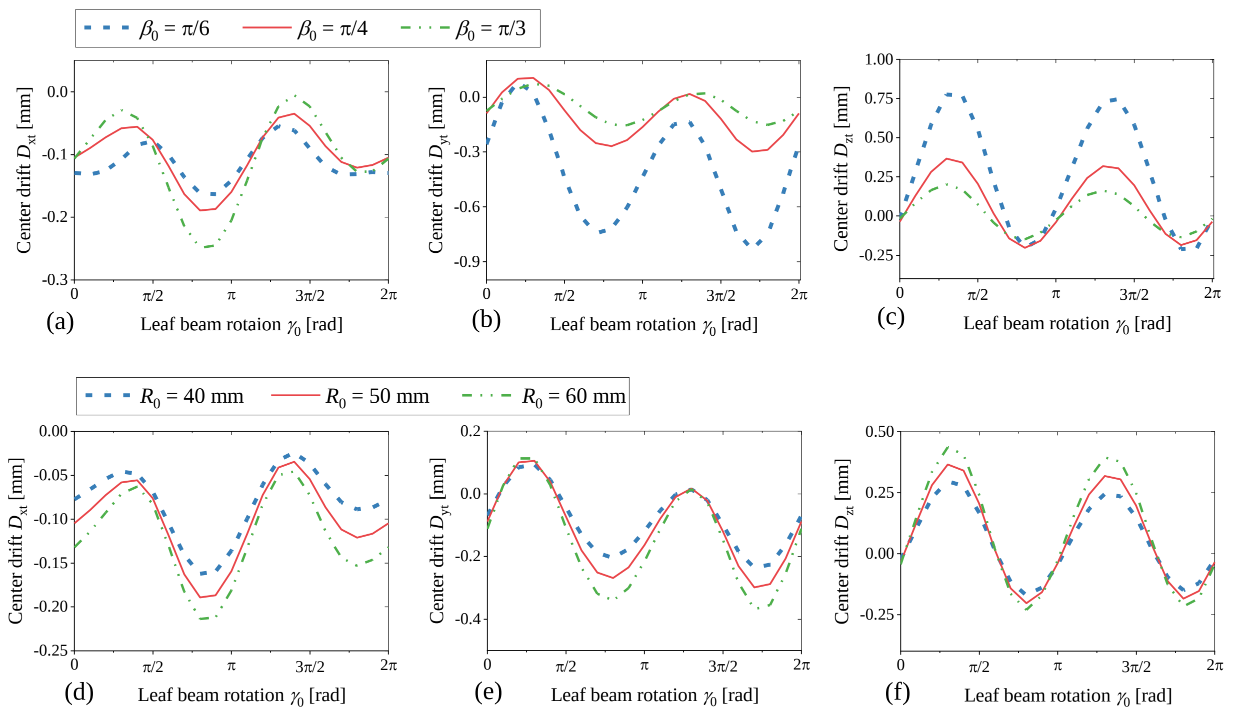

Figure 20 (Colour lines) The influence of geometry parameters γ_0, β_0, and R_0 on the center drift of the spherical joint with folded leaf beams under constant motion stage rotation (θ_{xt} = 0.2 rad, θ_{yt} = 0.3 rad and θ_{zt} = 0.5 rad): (a), (b), and (c) illustrate the incremental changes in γ_0 and β_0 with a constant R_0 value of 50 mm; (d), (e), and (f) showcase the incremental changes in γ_0 and R_0 with a constant β_0 value of π/4;

Table 2 Maximum centre drift comparison (γ_0 ranging from 0 to 2π and R_0 equals to 50 mm)

Spherical Joint	**Max D_x (mm)**			**Max D_y (mm)**			**Max D_z (mm)**		
	If β_0 equals to			If β_0 equals to			If β_0 equals to		
	π/6	π/4	π/3	π/6	π/4	π/3	π/6	π/4	π/3
I-shape	0.459	0.281	0.277	0.315	0.137	0.098	0.546	0.222	0.104
Non-orthogonal	0.461	0.289	0.311	0.503	0.294	0.191	0.710	0.331	0.210
L-shape	0.364	0.275	0.296	0.608	0.336	0.238	0.770	0.399	0.248
Folded	0.163	0.189	0.248	0.833	0.299	0.154	0.775	0.366	0.201

Table 2 summarizes the maximum centre drift of each spherical joint with γ_0 ranging from 0 to 2π radians and R_0 equal to 50 mm, under the loading conditions of $\theta_{xt} = 0.2$ rad, $\theta_{yt} = 0.3$ rad and $\theta_{zt} = 0.5$ rad. Notably, the spherical joint with folded leaf beams exhibits the lowest maximum centre drift in the X-direction, while the spherical joint with I-shape leaf beams demonstrates the lowest maximum centre drift in both the Y-direction and Z-direction. Conversely, the spherical joint with folded leaf beams yields the largest maximum centre drift, reaching 0.833 mm in the Y-direction. In contrast, the spherical joint with I-shape leaf beams achieves the lowest centre drift overall. Based on this data, it can be concluded that the spherical joint with I-shape leaf beams delivers the best performance, characterized by the smallest overall centre drift.

6. Experiment

The spherical joint with L-shaped leaf beams was selected for experimental testing due to its compact and simple configuration, which facilitates fabrication. Additionally, this configuration has not been experimentally investigated in previous literature, whereas spherical joints with I-shaped leaf beams and folded leaf beams have been studied in [7] and [33, 39], respectively. The study in this section will test both the force-displacement characteristics (including load-dependent effects) and the displacement-center drift relationships. The experimental results will be compared with the analytical and FEA results.

6.1 Fabrication of the prototype

Figure 21(a) illustrates the fabricated prototype, which includes non-deformable components such as the motion stage, intermediate stage, and base, being all fabricated using tough PLA filament through additive manufacturing. A 3D-printed pin using tough PLA (Polylactic Acid) is affixed to the motion stage, with its coloured tip serving as the remote centre of rotation for the spherical joint. A ruler with 0.1 mm resolution is placed on the base to provide a reference for the camera-based measurement of the pin tip position after each incremental displacement. The leaf beam is cut from a 0.3 mm thick stainless-steel sheet (Young's modulus: 200 GPa, Poisson's ratio: 0.33). The assembly is completed by inserting the leaf beams into the slotted non-deformable parts and bonding them with super glue. Detailed dimensions as defined in Figs. 8 and 1 of the fabricated prototypes are provided in Table 3.

Table 3 The geometry parameters of the spherical joint with L-shape leaf beams

Leaf beam in spherical joint	γ_0 **(rad)**	β_0 **(rad)**	R_0 **(mm)**	D **(mm)**	L **(mm)**	T **(mm)**	U **(mm)**
L-shape	0	π/4	55	9	50	0.3	12

6.2 Experimental hardware setup

The assembly of the experimental hardware setup consists of five primary sub-systems: the micrometer, force sensor, pulley system, fabricated prototype, and a macro camera, as shown in Fig. 21(b). The micrometer, with a resolution of 0.001 mm, is used for precise displacement actuation/input. The force sensor, with a resolution of 0.001 N and a range of 0 to 10 N, is aligned along the Y_T-direction to monitor reaction forces. The pulley system is employed to attach extra forces along the X_T-direction, simulating load-dependent effects on the spherical joint. The distance between the motion stage of the spherical joint and the pulley is intentionally set long enough to minimize loading misalignment during actuation, as illustrated in Fig. 21(c). The macro camera is used to capture the images of the pin tip and the ruler and enables the image-processing-based calculation of the pin tip position based on the reference ruler. By comparing these images at each incremental displacement, the movement of the pin tip (center drift) can be measured.

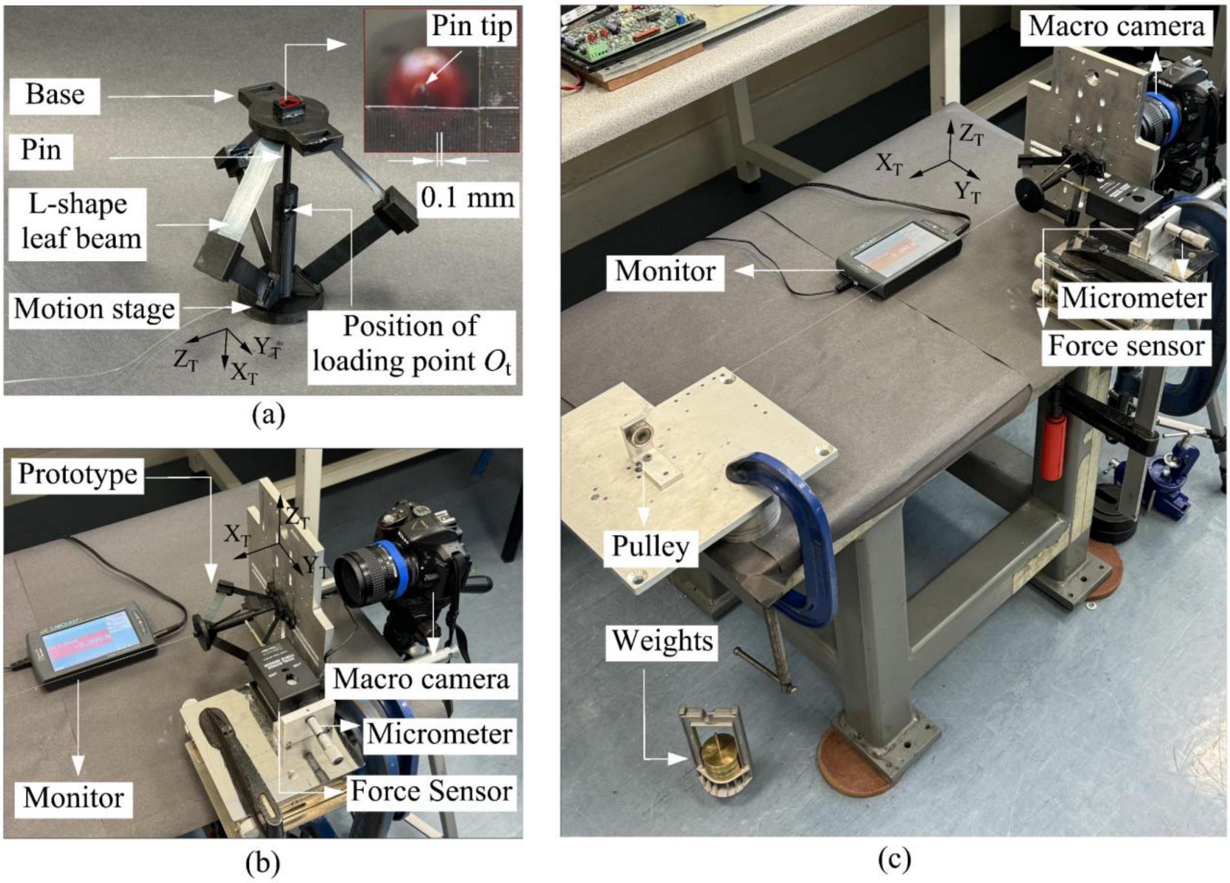

Figure 21 Experimental setup: (a) the spherical joint with L-shape leaf beams (pin tip is the remote centre P joint); (b) testing rig; (c) an overview of the experimental platform.

6.3 Experimental results

The experimental results are compared with FEA and analytical results to validate two key aspects of the spherical joint: the force-displacement relationship of the motion stage and the resultant center drift versus input displacement. As shown in Fig. 22(a), the experimental results align with both the FEA and analytical results, with a maximum error of 8.9%. The graph also demonstrates the expected nonlinear load-dependent effects where a larger axial force leads to a larger line slope (i.e., a larger rotational stiffness). Figures 22(b) and (c) show comparisons of the resultant center drift under incremental input displacements. Figure 22(b) compares the analytical results with the FEA results, while Figure 22(c) compares the analytical results with the experimental results. Both figures show the same nonlinear pattern of centre drift under different axial forces where the largest axial force results in the smallest centre drift. This finding means that the undesired centre drift can be further mitigated using axial loading on the spherical joint. It is also observed in Fig. 22(b) and (c) that the analytical results align more closely with the FEA results, with a maximum error of 11.2%, while deviating from the experimental results by a maximum error of 16.7%. Several factors could contribute to this deviation, including potential fabrication errors, assembly errors, and measurement errors, which are further elaborated below:

a) Fabrication errors primarily result from unintended elastic deformations of several parts (such as the motion stage) that were assumed to be rigid in the theoretical analysis.

b) Assembly errors may arise from the system misalignment between the pulley system and the motion stage, and the prototype inherent assembly error between the 3D printed part and the stainless-steel leaf beam.

c) Measurement errors can occur due to the use of a 0.1 mm resolution ruler for marking the position of the pin tip, which may not provide sufficient precision.

To prevent yield failure of the compliant spherical joint during experimental tests, the motion range before reaching the yield strength is determined based on the FEA simulation. From the FEA simulations, the maximum stress of the spherical joint prototype reaches the yield strength when the motion stage rotates 0.056 radians about the X-axis, 0.053 radians about the Y-axis, and 0.053 radians about the Z-axis. However, this stress aspect is not studied in the analytical model, as it is not the primary focus of this work. In both the experiment and the analytical model, the motion range is determined to voucher the maximum stress being far below the yield strength, which is a maximum rotation of approximately 0.047 radians about the Z-axis (equivalent to a 5-mm actuation/input displacement in the Y-axis). Under these conditions, experimental results show that the maximum center drift along the Y-axis reaches 0.22 mm.

From Fig. 22(b) and (c), we observe that the experimental center drift is approximately 22 times smaller than the displacement of the actuation point on the motion stage (reference point O_t as defined in Fig. 8) when the input displacement reaches 5 mm. Conversely, when the input displacement is around 1 mm, the experimental center drift is about 55 times smaller than the input displacement. This quantitatively demonstrates the nonlinear pattern of the centre drift: as the input displacement increases, the center drift increases exponentially.

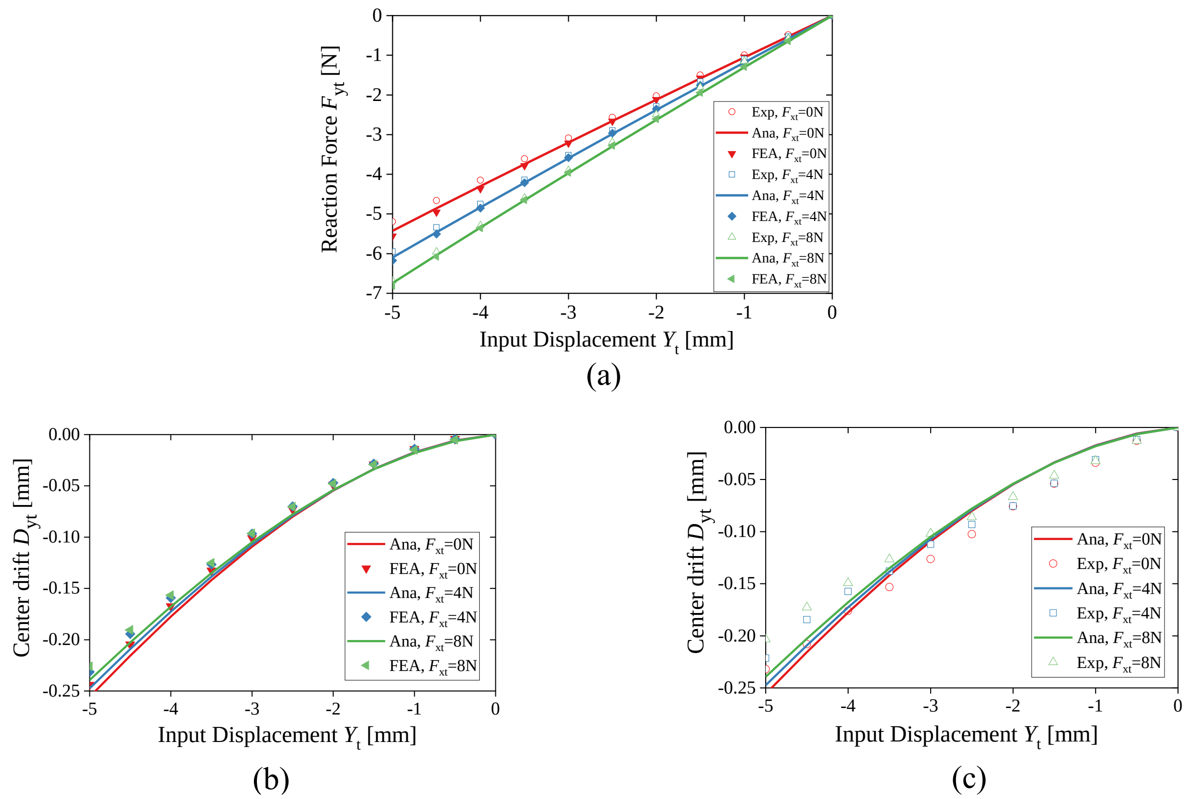

Figure 22 (Colour lines) Comparison of experimental, FEA, and analytical results: (a) force-displacement relationship of the motion stage; (b) centre drift analysis by comparing analytical and FEA results; (c) centre drift analysis by comparing analytical and experimental results.

While the compliant spherical joint does not achieve perfect precision as observed in the experiment, it offers several advantages over rigid-body remote centre of motion mechanisms. The absence of traditional joints enhances reliability and simplifies fabrication, reducing the need for precise assembly and alignment of multiple components. Additionally, compliant mechanisms inherently exhibit high repeatability and precision, as their motion is governed by material elasticity without backlash rather than mechanical tolerances. This makes them more robust against minor manufacturing imperfections.

It is worth noting that the spherical joint with L-shaped leaf beams can be further optimized to minimize center drift. In this study, the primary goal of the experiment was to validate the accuracy of the proposed model. Therefore, the prototype parameters were chosen to facilitate fabrication and experimental measurement rather than to achieve optimal precision performance.

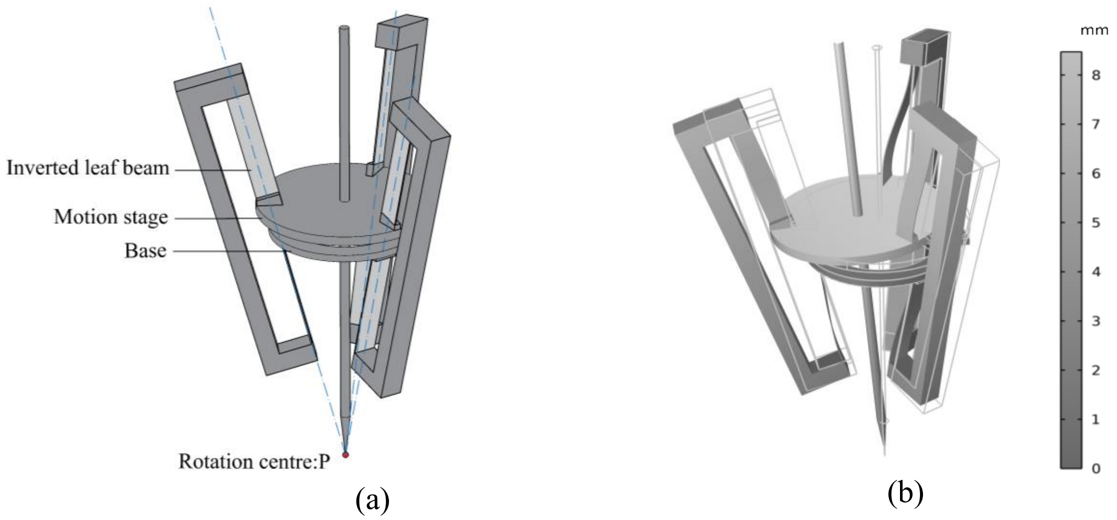

Figure 23 Spherical joint with inverted single-translation constraint: (a) the sketch of the geometry; (b) the deformed configuration.

7. Further discussions

7.1 Other associated designs

Interesting spherical joints can be designed using the GSTC leaf beams. In Fig. 23(a), we observe the spherical joint featuring inverted leaf beams. This design boasts remarkable load-bearing capacity owing to the inherent anti-buckling property of the inverted leaf beam [40, 41]. In Figure 23(b), the deformed configuration of the spherical joint under a force in the Y_T-axis is illustrated. While the standard case defines β_{xi} = 90 degrees for the aforementioned spherical joint with I-shape leaf beams, other exceptions exist, as shown in Fig. 24 where β_{xi} equals 45 degrees (Fig. 1). Despite this deviation, the joint still retains its spherical characteristics. However, the three embodied 45-degree I-shape leaf beams exhibit strong coupling relationships, resulting in heightened stiffness in all directions. This may pose a drawback, necessitating a higher actuation force. The deformed configuration of the spherical joint is shown in Fig. 24(b).

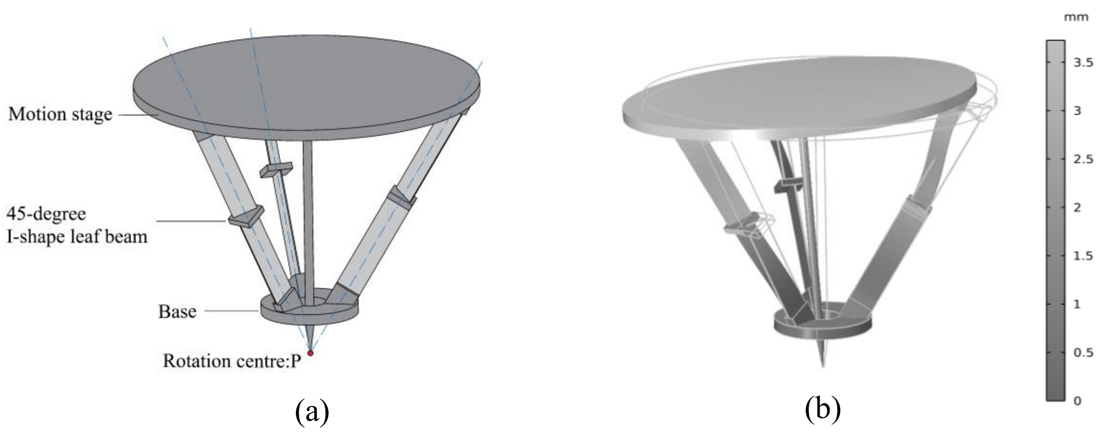

Figure 24 Spherical joint with 45-degree I-shape leaf beams: (a) the sketch of the geometry; (b) the deformed configuration.

7.2 Model errors

The obtained spatial kinetostatic models for the general spherical joint and the GSTC leaf beam contain source errors from the SBCM [24, 25]. On the one hand, the SBCM is based on the Euler-Bernoulli beam assumption that disregards the shear effect. In the case of stubby beams, the model error could be significant. To address this issue, the Timoshenko beam theory, which accounts for the effect of shear strains in a beam and adds a correction term to the Euler-Bernoulli beam theory, can be used. On the other hand, the SBCM can introduce truncation errors due to the resulting closed-form solutions [8].

Moreover, during the FEA verification of the force-displacement characteristics of the GSTC leaf beam or the spherical joint, we observed that errors tend to be more pronounced when the resultant translation or rotations are small. This may be caused by numerical precision limitations. In FEA, the finite element method involves approximations and numerical calculations, which can introduce rounding errors. When the results are small, these errors can be significant relative to the magnitude of the result. Despite this, such inaccuracies in FEA are considered acceptable. Additionally, applying boundary conditions, including forces or displacements, which enable substantial movements in all directions simultaneously can be challenging in FEA, whereas this is more straightforward in analytical models. An understanding of the above issues can help us better interpret the observed differences between the FEA and analytical models.

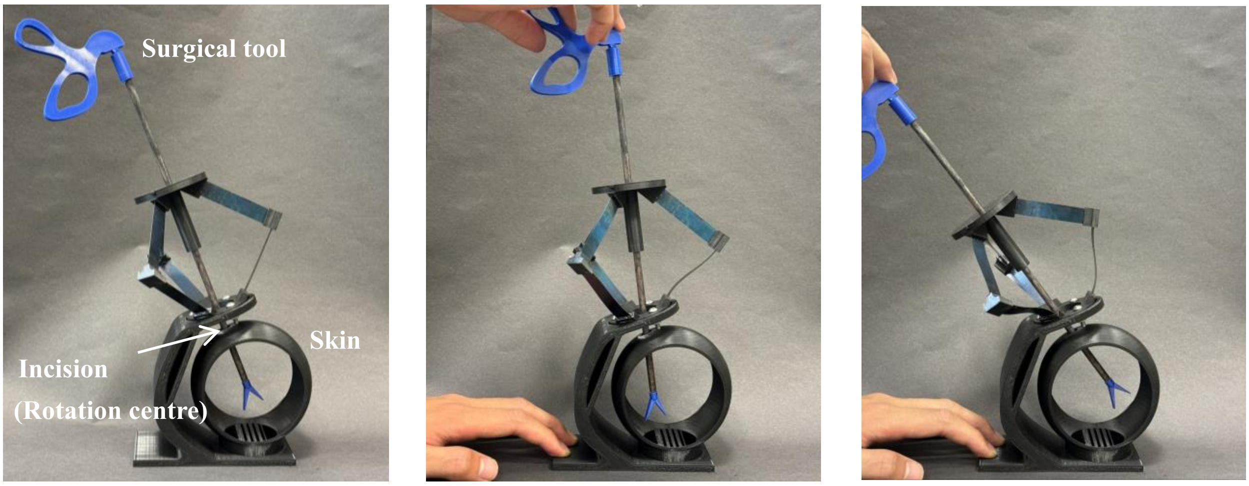

Figure 25 Demonstration of the spherical joint in the application of minimally invasive surgery

7.3 Demonstrated application and other prototypes

The spherical joint is a versatile element with broad applications in fields such as compliant parallel robots and minimally invasive surgery. Its design flexibility makes it particularly suitable for environments that require precision, compactness, and material efficiency. Figure 25 illustrates an example of the spherical joint integrated with L-shaped leaf springs, tailored for use in minimally invasive surgical procedures.

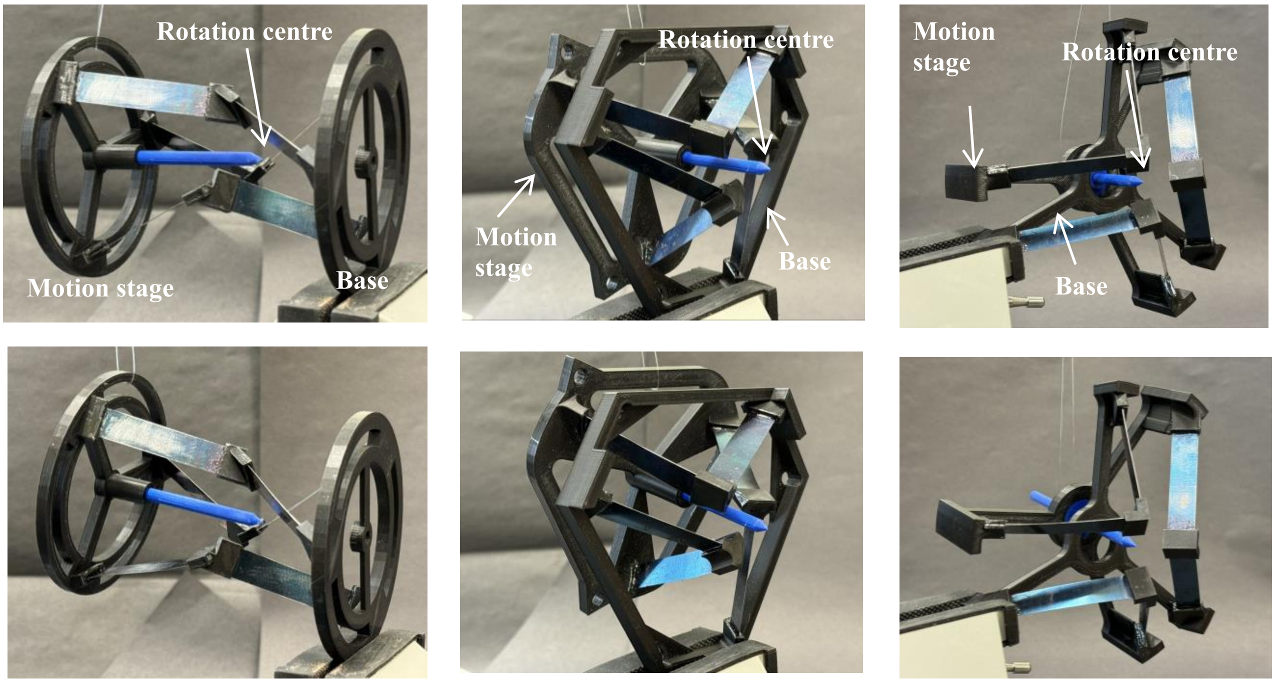

(a) (b) (c)

Figure 26 Other prototypes: (a) the spherical joint with non-orthogonal leaf beams; (b) the spherical joint with L-shape leaf beams; (c) the spherical joint with folded-leaf beams.

Several other prototypes, showcased in Fig. 26, have been fabricated to further explore the potential of the proposed general spherical joint. These prototypes have demonstrated promising results, achieving the goals of material conservation and simplified fabrication. Moreover, the designs can be made more compact, making them ideal for use in confined spaces, such as those encountered in surgical or robotic applications.

8. Conclusions

This paper has proposed the design of a GSTC leaf beam, which offers versatility in designing various single-translation constraint leaf beams. The spatial kinetostatic model of the GSTC leaf beam is derived using a nonlinear SBCM, which was not reported in the prior art. The spatial kinetostatic model of the GSTC leaf beam is comprehensively verified using the nonlinear FEA solver.

Furthermore, a general design of a spherical joint is proposed by using three identical GSTC leaf beams. The spatial kinetostatic model of the general spherical joint with GSTC leaf beams has been rigorously developed. Several representative spherical joints have been selected for FEA verification and comparative analysis and, including the spherical joint with non-orthogonal leaf beams, that with I-shape leaf beams, that with L-shape leaf beams, and that with folded leaf beams. Based on the proposed spatial kinetostatic model, the influence of major structure geometric parameters on the center drift is fully examined. The comparison of the maximum center drifts in each direction shows that the spherical joint with I-shape leaf beams generally has better performance. An experiment using the spherical joint with L-shape leaf beams was conducted to validate the force-displacement relationship of the motion stage and the resultant center drift under incremental input displacement. The experimental results confirmed the high accuracy of the nonlinear spatial kinetostatic models mentioned above, demonstrating their potential for facilitating model-based, quick multi-objective optimization in the future.

Our future work will focus on the nonlinear support stiffness analysis of the general spherical joints as well as the model-based multi-objective optimization to minimize the centre drift.

Acknowledgments

Jiaxiang Zhu is grateful for the financial support from the China Scholarship Council (CSC Student ID: 202008300013).

Declaration of Competing Interest

The authors declare that they have no known competing financial interests or personal relationships that could have appeared to influence the work reported in this paper.

References

[1] Howell, L. L., 2013, Compliant mechanisms, In *21st century kinematics*, pp. 189-216. Springer. https://doi.org/10.1007/978-1-4471-4510-3_7

[2] Liu, P., and Yan, P. J. M. S., 2017, A modified pseudo-rigid-body modeling approach for compliant mechanisms with fixed-guided beam flexures, *Mechanical Sciences,* 8 (2), pp. 359-368. https://doi.org/10.5194/ms-8-359-2017

[3] Soemers, H. M., 2010, *Design principles for precision mechanisms*, University of Twente.

[4] Dan, W., and Rui, F., 2016, Design and nonlinear analysis of a 6-DOF compliant parallel manipulator with spatial beam flexure hinges, *Precision Engineering,* 45, pp. 365-373. https://doi.org/10.1016/j.precisioneng.2016.03.013

[5] Hao, G., and Kong, X. J. M. S., 2016, A structure design method for compliant parallel manipulators with actuation isolation, *Mechanical Sciences,* 7, pp. 247-253. https://doi.org/10.5194/ms-7-247-2016

[6] Howell, L. L., Magleby, S. P., and Olsen, B. M., 2013, *Handbook of Compliant Mechanisms*, Wiley. New York. 10.1002/9781118516485

[7] Hao, G., He, X., Zhu, J., and Li, H., 2024, Design and Analysis of Leaf Beam Single-Translation Constraint Compliant Modules and the Resulting Spherical Joints, *Journal of Mechanical Design,* 146 (8). https://doi.org/10.1115/1.4064415

[8] Awtar, S., Slocum, A. H., and Sevincer, E., 2006, Characteristics of Beam-Based Flexure Modules, *Journal of Mechanical Design,* 129 (6), pp. 625-639. https://doi.org/10.1115/1.2717231

[9] Awtar, S., and Sen, S., 2010, A Generalized Constraint Model for Two-Dimensional Beam Flexures: Nonlinear Strain Energy Formulation, *Journal of Mechanical Design,* 132 (8), pp. 081009. https://doi.org/10.1115/1.4002006

[10] Howell, L. L., Midha, A., and Norton, T. W., 1996, Evaluation of Equivalent Spring Stiffness for Use in a Pseudo-Rigid-Body Model of Large-Deflection Compliant Mechanisms, *Journal of Mechanical Design,* 118 (1), pp. 126-131. https://doi.org/10.1115/1.2826843

[11] Howell, L. L., and Midha, A., 1994, A Method for the Design of Compliant Mechanisms With Small-Length Flexural Pivots, *Journal of Mechanical Design,* 116 (1), pp. 280-290. https://doi.org/10.1115/1.2919359

[12] Su, H.-J., 2009, A Pseudorigid-Body 3R Model for Determining Large Deflection of Cantilever Beams Subject to Tip Loads, *Journal of Mechanisms and Robotics,* 1 (2). https://doi.org/10.1115/1.3046148

[13] Yu, Y.-Q., Feng, Z.-L., and Xu, Q.-P., 2012, A pseudo-rigid-body 2R model of flexural beam in compliant mechanisms, *Mechanism and Machine Theory,* 55, pp. 18-33. https://doi.org/10.1016/j.mechmachtheory.2012.04.005

[14] Ma, F., and Chen, G., 2014, Chained Beam-Constraint-Model (CBCM): a powerful tool for modeling large and complicated deflections of flexible beams in compliant mechanisms, *International Design Engineering Technical Conferences and Computers and Information in Engineering Conference*, pp. V05AT08A027. https://doi.org/10.1115/DETC2014-34140

[15] Pauly, J., and Midha, A., 2006, Pseudo-Rigid-Body Model Chain Algorithm: Part 1 — Introduction and Concept Development, *ASME 2006 International Design Engineering Technical Conferences and Computers and Information in Engineering Conference*, pp. 173-181. https://doi.org/10.1115/DETC2006-99460

[16] Jin, M., Yang, Z., Ynchausti, C., Zhu, B., Zhang, X., and Howell, L. L., 2020, Large-Deflection Analysis of General Beams in Contact-Aided Compliant Mechanisms Using Chained Pseudo-

Rigid-Body Model, *Journal of Mechanisms and Robotics,* 12 (3). https://doi.org/10.1115/1.4045425

[17] Sen, S., and Awtar, S., 2013, A Closed-Form Nonlinear Model for the Constraint Characteristics of Symmetric Spatial Beams, *Journal of Mechanical Design,* 135 (3). https://doi.org/10.1115/1.4023157

[18] Sen, S., and Awtar, S., 2014, Nonlinear Strain Energy Formulation of a Generalized Bisymmetric Spatial Beam for Flexure Mechanism Analysis, *J Mech Des N Y,* 136 (2), pp. 0210021-2100213. https://doi.org/10.1115/1.4025705

[19] Rasmussen, N. O., Wittwer, J. W., Todd, R. H., Howell, L. L., and Magleby, S. P., 2006, A 3d pseudo-rigid-body model for large spatial deflections of rectangular cantilever beams, *International Design Engineering Technical Conferences and Computers and Information in Engineering Conference*, pp. 191-198. https://doi.org/10.1115/DETC2006-99465

[20] Chase Jr, R. P., Todd, R. H., Howell, L. L., and Magleby, S., 2011, A 3-D chain algorithm with pseudo-rigid-body model elements, *Mechanics Based Design of Structures and Machines,* 39 (1), pp. 142-156. https://doi.org/10.1080/15397734.2011.541783

[21] Chimento, J., Lusk, C., and Alqasimi, A., 2014, A 3-D pseudo-rigid body model for rectangular cantilever beams with an arbitrary force end-load, *International Design Engineering Technical Conferences and Computers and Information in Engineering Conference*, pp. V05AT08A029. https://doi.org/10.1115/DETC2014-34292

[22] Nijenhuis, M., Meijaard, J. P., Mariappan, D., Herder, J. L., Brouwer, D. M., and Awtar, S., 2017, An Analytical Formulation for the Lateral Support Stiffness of a Spatial Flexure Strip, *Journal of Mechanical Design,* 139 (5). https://doi.org/10.1115/1.4035861

[23] Nijenhuis, M., Meijaard, J. P., and Brouwer, D. M., 2020, A spatial closed-form nonlinear stiffness model for sheet flexures based on a mixed variational principle including third-order effects, *Precision Engineering,* 66, pp. 429-444. https://doi.org/10.1016/j.precisioneng.2020.08.003

[24] Bai, R., Awtar, S., and Chen, G., 2019, A closed-form model for nonlinear spatial deflections of rectangular beams in intermediate range, *International Journal of Mechanical Sciences,* 160, pp. 229-240. https://doi.org/10.1016/j.ijmecsci.2019.06.042

[25] Bai, R., Chen, G., and Awtar, S., 2021, Closed-form solution for nonlinear spatial deflections of strip flexures of large aspect ratio considering second order load-stiffening, *Mechanism and Machine Theory,* 161. https://doi.org/10.1016/j.mechmachtheory.2021.104324

[26] Bai, R., Yang, N., Li, B., and Chen, G., 2024, Nonlinear strain energy formulation of spatially deflected strip flexures, *Mechanism and Machine Theory,* 195. https://doi.org/10.1016/j.mechmachtheory.2024.105594

[27] Hao, G., Kong, X., and Reuben, R. L., 2011, A nonlinear analysis of spatial compliant parallel modules: Multi-beam modules, *Mechanism and Machine Theory,* 46 (5), pp. 680-706. https://doi.org/10.1016/j.mechmachtheory.2010.12.007

[28] Slabaugh, G. G., 1999, Computing Euler angles from a rotation matrix, *Retrieved on August 6,* 6 (2000), pp. 39-63.

[29] Morawiec, A., 2003, *Orientations and rotations*, Springer.

[30] Den Hartog, J. P., 1987, *Advanced strength of materials*, Courier Corporation.

[31] Awtar, S., 2003, *Synthesis and Analysis of Parallel Kinematic XY Flexure Mechanisms*, *PhD diss., Massachusetts Institute of Technology*. Cambridge, MA.

[32] Archer, R. R., Crandall, S. H., Dahl, N. C., and Lardner, T. J. J., 1959, *An introduction to the mechanics of solids*. McGraw-Hill, New York.

[33] Naves, M., Aarts, R. G. K. M., and Brouwer, D. M., 2019, Large stroke high off-axis stiffness three degree of freedom spherical flexure joint, *Precision Engineering,* 56, pp. 422-431. https://doi.org/10.1016/j.precisioneng.2019.01.011

[34] Schellekens, P., Rosielle, N., Vermeulen, H., Vermeulen, M., Wetzels, S., and Pril, W. J. C. A., 1998, Design for precision: current status and trends, 47 (2), pp. 557-586. https://doi.org/10.1016/S0007-8506(07)63243-0

[35] Zhu, J., and Hao, G., 2023, Modelling of a general lumped-compliance beam for compliant mechanisms, *International Journal of Mechanical Sciences*. https://doi.org/10.1016/j.ijmecsci.2023.108779

[36] Li, S., and Hao, G., 2022, Design and nonlinear spatial analysis of compliant anti-buckling universal joints, *International Journal of Mechanical Sciences,* 219. https://doi.org/10.1016/j.ijmecsci.2022.107111

[37] Hao, G., and Kong, X., 2013, A normalization-based approach to the mobility analysis of spatial compliant multi-beam modules, *Mechanism and Machine Theory,* 59, pp. 1-19. https://doi.org/10.1016/j.mechmachtheory.2012.08.013

[38] Lobontiu, N., 2002, *Compliant mechanisms: design of flexure hinges*, CRC press. https://doi.org/10.1201/9781420040272

[39] Rommers, J., Naves, M., Brouwer, D. M., and Herder, J. L., 2021, A Flexure-Based Linear Guide With Torsion Reinforcement Structures, *Journal of Mechanisms and Robotics,* 14 (3). https://doi.org/10.1115/1.4052971

[40] Hao, G., and Zhu, J., 2019, Design of a Monolithic Double-Slider Based Compliant Gripper with Large Displacement and Anti-Buckling Ability, *Micromachines (Basel),* 10 (10). https://doi.org/10.3390/mi10100665

[41] Masters, N. D., and Howell, L. L., 2003, A self-retracting fully compliant bistable micromechanism, *Journal of Microelectromechanical Systems,* 12 (3), pp. 273-280. https://doi.org/10.1109/jmems.2003.811751

Appendix A: The nonlinear spatial beam constraint model of a leaf beam

Each of the leaf beams is kinetostatically modelled using the nonlinear spatial beam constraint model (SBCM) as reported in [24]. This modelling approach is capable of accurately capturing the nonlinear effects such as load-stiffening and elastokinematic nonlinearities over the intermediate deflection range defined as 10% of the beam length. It provides closed-form solutions for the force-displacement characteristics at the tip of the leaf beam under a general loading condition. Below is an example of leaf beam 1 subjected to such a condition (Fig. A1), followed by the closed-form solution for SBCM of leaf beam 1.

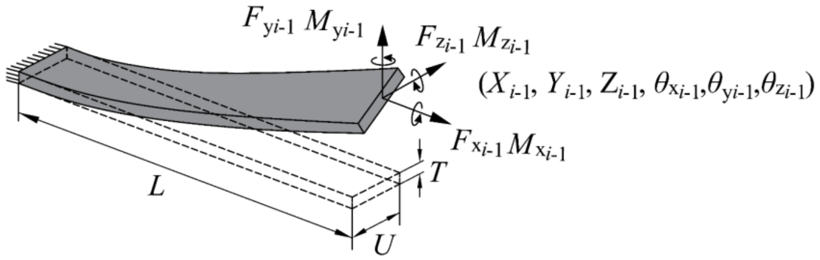

Figure A1 Description of leaf beam 1 subjected to a general loading condition and its resulting displacements

$$\begin{bmatrix} f_{yi-1} \\ m_{zi-1} \\ m_{xi-1} \end{bmatrix} = H_1 \begin{bmatrix} y_{i-1} \\ \theta_{zi-1} \\ \theta_{xi-1} \end{bmatrix} + \left(f_{xi-1}H_2 + f_{zi-1}H_3 + m_{yi-1}H_4 \right) \begin{bmatrix} y_{i-1} \\ \theta_{zi-1} \\ \theta_{xi-1} \end{bmatrix} + \left(f_{xi-1}^2 H_5 + f_{zi-1}^2 H_6 + f_{zi-1} m_{yi-1} H_7 + m_{yi-1}^2 H_8 \right) \begin{bmatrix} y_{i-1} \\ \theta_{zi-1} \\ \theta_{xi-1} \end{bmatrix} \quad \text{(A.1)}$$

$$z_{i-1} = f_{zi-1}\left(\frac{r}{3} + \frac{1}{\kappa k_s} \right) - \frac{m_{yi-1} r}{2} + \begin{bmatrix} f_{zi-1} & m_{yi-1} & f_{xi-1} \end{bmatrix} C_1 \begin{bmatrix} f_{zi-1} \\ m_{yi-1} \\ f_{xi-1} \end{bmatrix} - \begin{bmatrix} y_{i-1} & \theta_{zi-1} & \theta_{xi-1} \end{bmatrix} (H_3 / 2) \begin{bmatrix} y_{i-1} \\ \theta_{zi-1} \\ \theta_{xi-1} \end{bmatrix} \quad \text{(A.2)}$$

$$- \begin{bmatrix} y_{i-1} & \theta_{zi-1} & \theta_{xi-1} \end{bmatrix} \left(f_{zi-1}H_6 + m_{yi-1}H_7 / 2 + f_{xi-1} f_{zi-1} C_2 + f_{xi-1} m_{yi-1} C_3 \right) \begin{bmatrix} y_{i-1} \\ \theta_{zi-1} \\ \theta_{xi-1} \end{bmatrix}$$

$$\theta_{yi} = -\frac{f_{zi-1} r}{2} + m_{yi-1} r + \begin{bmatrix} f_{zi-1} & m_{yi-1} & f_{xi-1} \end{bmatrix} C_4 \begin{bmatrix} f_{zi-1} \\ m_{yi-1} \\ f_{xi-1} \end{bmatrix} - \begin{bmatrix} y_{i-1} & \theta_{zi-1} & \theta_{xi-1} \end{bmatrix} (H_4 / 2 + H_9) \begin{bmatrix} y_{i-1} \\ \theta_{zi-1} \\ \theta_{xi-1} \end{bmatrix} \quad \text{(A.3)}$$

$$- \begin{bmatrix} y_{i-1} & \theta_{zi-1} & \theta_{xi-1} \end{bmatrix} \left(f_{zi-1}H_7 / 2 + m_{yi-1}H_8 + f_{xi-1} f_{zi-1} C_5 + f_{xi-1} m_{yi-1} C_6 \right) \begin{bmatrix} y_{i-1} \\ \theta_{zi-1} \\ \theta_{xi-1} \end{bmatrix}$$

$$z_{i-1} = \frac{f_{xi-1}}{k_a} - \begin{bmatrix} y_{i-1} & \theta_{zi-1} & \theta_{xi-1} \end{bmatrix} (H_2 / 2 + f_{xi-1} H_5) \begin{bmatrix} y_{i-1} \\ \theta_{zi-1} \\ \theta_{xi-1} \end{bmatrix} \quad \text{(A.4)}$$

where $f_{xi\text{-}1}$, $f_{yi\text{-}1}$, $f_{zi\text{-}1}$, $m_{xi\text{-}1}$, $m_{yi\text{-}1}$ and $m_{zi\text{-}1}$ donate the forces and moments of the tip flexure beam 1, and the resultant displacements are $x_{i\text{-}1}$, $y_{i\text{-}1}$, $z_{i\text{-}1}$, $\theta_{xi\text{-}1}$, $\theta_{yi\text{-}1}$ and $\theta_{zi\text{-}1}$ as shown in Fig. A1. A similar labelling pattern applies to flexure beam 2. i donate the i^{th} *GSTC* leaf beam; I_y denotes the cross-section moment of inertia about the y_i-axis, which is expressed as $I_y = TU^3/12$; $\kappa = 10(1+v)/(12+11v)$; $k_a = UTL^2/I_z$; $k_t = GJ/(EI_z)$; $k_s = GUTL2/(EI_z)$; $r = I_z/I_y$.

The coefficients H_1 through H_9, C_1 through C_5, and J are formulated as Eqs. (A.5) through (A.7), respectively.

$$H_1=\begin{bmatrix}12&-6&0\\-6&4&0\\0&0&k_t\end{bmatrix};H_2=\begin{bmatrix}1.2&-0.1&0\\-0.1&2/15&0\\0&0&0\end{bmatrix};H_3=\begin{bmatrix}0&0&0\\0&0&-1/6\\0&-1/6&0\end{bmatrix};H_4=\begin{bmatrix}0&0&-1\\0&0&1\\-1&0&0\end{bmatrix}; \tag{A.5}$$

$$H_5=\begin{bmatrix}-1/700&1/1400&0\\1/1400&-11/6300&0\\0&0&0\end{bmatrix};H_6=\frac{1}{k_t}\begin{bmatrix}-3/35&1/105&0\\1/105&-13/1260&0\\0&0&-1/180\end{bmatrix};$$

$$H_7=\frac{1}{k_t}\begin{bmatrix}1/5&-1/30&0\\-1/30&1/15&0\\0&0&0\end{bmatrix};H_8=\frac{1}{k_t}\begin{bmatrix}-1/5&1/10&0\\1/10&-2/15&0\\0&0&0\end{bmatrix};H_9==\begin{bmatrix}0&0&0\\0&0&0\\0&1&0\end{bmatrix};$$

$$C_1=\begin{bmatrix}0&0&-\frac{r^2}{15}\\0&0&\frac{5r^2}{48}\\-\frac{r^2}{15}&\frac{5r^2}{48}&0\end{bmatrix};C_2=\begin{bmatrix}\frac{415r+14}{12600k_t}&-\frac{245r+6}{50400k_t}&0\\-\frac{245r+6}{50400k_t}&\frac{235r+8}{12600k_t}&0\\0&0&0\end{bmatrix};C_3=\begin{bmatrix}-\frac{40r+1}{700k_t}&\frac{30r+1}{600k_t}&0\\\frac{30r+1}{600k_t}&-\frac{410r+33}{50400k_t}&0\\0&0&0\end{bmatrix}; \tag{A.6}$$

$$C_4=\begin{bmatrix}0&0&\frac{5r^2}{48k_t}\\0&0&-\frac{r^2}{6}\\\frac{5r^2}{48k_t}&-\frac{r^2}{6}&0\end{bmatrix};C_5=\begin{bmatrix}-\frac{35r+1}{700k_t}&\frac{403r+7}{4200k_t}&0\\\frac{403r+7}{4200k_t}&-\frac{835r+103}{25200k_t}&0\\0&0&0\end{bmatrix};C_6=\begin{bmatrix}\frac{4r+1}{350k_t}&-\frac{190r+3}{2100k_t}&0\\-\frac{190r+3}{2100k_t}&\frac{175r+22}{6300k_t}&0\\0&0&0\end{bmatrix};$$

$$J=\frac{2\cdot T^3\cdot U^3}{7\cdot T^2+7\cdot U^2}\cdot\left(\frac{1.167\cdot\eta^5+29.49\cdot\eta^4+30.9\cdot\eta^3+100.9\cdot\eta^2+30.38\cdot\eta+29.41}{\eta^5+25.91\cdot\eta^4+41.58\cdot\eta^3+90.43\cdot\eta^2+41.74\cdot\eta+25.21}\right); \tag{A.7}$$

Appendix B: Force-equilibrium equations and geometry compatibility conditions of the GSTC leaf beam

This appendix presents the force-equilibrium equations and geometry compatibility conditions for the GSTC leaf beam. The force-equilibrium equations are derived based on the free-body diagram (FBD) in the deformed configuration, mainly accounting for the contributions of the axial load to the bending moment. The geometry-compatibility conditions are kinematic relationships that adhere to the geometric constraints defined in this paper, which are also derived under the deformed condition.

$$\begin{aligned}&\left[f_{\mathrm{x}i-2}, f_{\mathrm{y}i-2}, f_{\mathrm{z}i-2}, m_{\mathrm{x}i-2}, m_{\mathrm{x}i-2}, m_{\mathrm{x}i-2}\right]^{\mathrm{T}} = D_{\mathrm{S}i}^{\mathrm{T}} R_{\mathrm{SY}i} R_{\mathrm{S}i} R_{\mathrm{SY}i}^{\mathrm{T}} R_{\mathrm{SZ}i} R_{\mathrm{SX}i} \left[f_{\mathrm{x}i-1}, f_{\mathrm{y}i-1}, f_{\mathrm{z}i-1}, m_{\mathrm{x}i-1}, m_{\mathrm{x}i-1}, m_{\mathrm{x}i-1}\right]^{\mathrm{T}};\\ &\left[f_{\mathrm{xs}i}, f_{\mathrm{ys}i}, f_{\mathrm{zs}i}, m_{\mathrm{xs}i}, m_{\mathrm{ys}i}, m_{\mathrm{zs}i}\right]^{\mathrm{T}} = R_{\mathrm{SY}i} R_{\mathrm{S}i} R_{\mathrm{SY}i}^{\mathrm{T}} R_{\mathrm{SZ}i} R_{\mathrm{SX}i} \left[f_{\mathrm{x}i-1}, f_{\mathrm{y}i-1}, f_{\mathrm{z}i-1}, m_{\mathrm{x}i-1}, m_{\mathrm{x}i-1}, m_{\mathrm{x}i-1}\right]^{\mathrm{T}};\end{aligned} \tag{B.1}$$

where $f_{\mathrm{x}i\text{-}1}, f_{\mathrm{y}i\text{-}1}, f_{\mathrm{z}i\text{-}1}$, $m_{\mathrm{x}i\text{-}1}$, $m_{\mathrm{y}i\text{-}1}$ and $m_{\mathrm{z}i\text{-}1}$ donate the forces and moments of the tip of leaf beam 1, and the resultant displacements are $x_{i\text{-}1}$, $y_{i\text{-}1}$, $z_{i\text{-}1}$, $\theta_{xi\text{-}1}$, $\theta_{yi\text{-}1}$ and $\theta_{zi\text{-}1}$. A similar labelling pattern applies to leaf beam 2. The matrix $D_{\mathrm{S}i}$ donates a 6×6 normalised translational matrix for the tip of the GSTC leaf beam module, as provided below. $R_{\mathrm{S}i}$ donates rotational matrix for the tip GSTC leaf beam. When multiplied by the force represented in the global coordinate system, it yields the moments created by the forces in the deformed configuration. All forces and moments are expressed with respect to the global coordinate system X_S-Y_S-Z_S, achieved by multiplying the transformation matrices, namely $R_{\mathrm{SX}i}$, $R_{\mathrm{SY}i}$ and $R_{\mathrm{SZ}i}$.

$$\begin{aligned}&R_{\mathrm{S}i} = \begin{bmatrix} R_{\mathrm{s}i} & 0_{3\times3} \\ 0_{3\times3} & R_{\mathrm{s}i} \end{bmatrix};\ R_{\mathrm{SY}i} = \begin{bmatrix} R_{\mathrm{y}i} & 0_{3\times3} \\ 0_{3\times3} & R_{\mathrm{y}i} \end{bmatrix};\ R_{\mathrm{SZ}i} = \begin{bmatrix} R_{\mathrm{z}i} & 0_{3\times3} \\ 0_{3\times3} & R_{\mathrm{z}i} \end{bmatrix};\ R_{\mathrm{SX}i} = \begin{bmatrix} R_{\mathrm{x}i} & 0_{3\times3} \\ 0_{3\times3} & R_{\mathrm{x}i} \end{bmatrix};\\ &R_{xi} = \begin{bmatrix} 1 & 0 & 0 \\ 0 & \cos(\beta_{xi}) & -\sin(\beta_{xi}) \\ 0 & \sin(\beta_{xi}) & \cos(\beta_{xi}) \end{bmatrix}; R_{yi} = \begin{bmatrix} \cos(\beta_{yi}) & 0 & \sin(\beta_{yi}) \\ 0 & 1 & 0 \\ -\sin(\beta_{yi}) & 0 & \cos(\beta_{yi}) \end{bmatrix}; R_{zi} = \begin{bmatrix} \cos(\beta_{zi}) & -\sin(\beta_{zi}) & 0 \\ \sin(\beta_{zi}) & \cos(\beta_{zi}) & 0 \\ 0 & 0 & 1 \end{bmatrix};\end{aligned} \tag{B.2}$$

$$D_{\mathrm{S}i} = \begin{bmatrix} I_{3\times3} & \begin{matrix} 0 & A^*(3,1) & -A^*(2,1) \\ -A^*(3,1) & 0 & A^*(1,1) \\ A^*(2,1) & -A^*(1,1) & 0 \end{matrix} \\ 0_{3\times3} & I_{3\times3} \end{bmatrix}; \tag{B.3}$$

where $I_{3\times3}$ donates a 3×3 identity matrix, while $0_{3\times3}$ donates a zero matrix. A^* donates a 3×3 matrix which represents the deformed position of the tip of the GSTC leaf beam with respect to the global coordinate X_S-Y_S-Z_S. The expression is presented below.

$$A^* = R_{yi}R_{si}\left[\cos\beta_{yi}(\cos\beta_{zi}l+\cos\beta_{yi}d),\ \sin\beta_{zi}(d+l),\ \cos\beta_{zi}\sin\beta_{yi}(d+l)\right]^{\mathrm{T}} + R_{yi}R_{si}R_{yi}^{\mathrm{T}}R_{zi}R_{xi}\left[x_{i-1},\ y_{i-1},\ z_{i-1}\right]^{\mathrm{T}}; \tag{B.4}$$

The geometry compatibility for the GSTC leaf beam is derived based on its deformed configuration, as detailed below.

$$\begin{aligned}\left[x_{si},\ y_{si},\ z_{si}\right]^{\mathrm{T}} &= R_{yi}\left[x_{i-2},\ y_{i-2},\ z_{i-2}\right]^{\mathrm{T}} + R_{yi}R_{si}R_{yi}^{\mathrm{T}}R_{zi}R_{xi}\left[x_{i-1},\ y_{i-1},\ z_{i-1}\right]^{\mathrm{T}} \\ &+R_{yi}(R_{si}(\left[\cos\beta_{yi}(\cos\beta_{zi}l+\cos\beta_{yi}d),\ \sin\beta_{zi}(d+l),\ \cos\beta_{zi}\sin\beta_{yi}(d+l)\right]^{\mathrm{T}} - I_{3\times1}));\end{aligned} \tag{B.5}$$

$$\left[\theta_{xsi},\ \theta_{ysi},\ \theta_{zsi}\right]^{\mathrm{T}} = R_{yi}\left[\theta_{xi-2},\ \theta_{yi-2},\ \theta_{zi-2}\right]^{\mathrm{T}} + R_{yi}R_{si}R_{yi}^{\mathrm{T}}R_{zi}R_{xi}\left[\theta_{xi-1},\ \theta_{yi-1},\ \theta_{zi-1}\right]^{\mathrm{T}}; \tag{B.6}$$

where R_{si} donates the 3×3 rotational matrix for the tip GSTC leaf beam. R_{xi}, R_{yi} and R_{zi} donate the 3×3 rotational matrices about the X-axis, Y-axis, and Z-axis, respectively.

Appendix C: The deformed configuration of the spherical joints in FEA

In Sec. 4.1, four specific spherical joints are studied. The deformation of each spherical joint in FEA under combined forces and moments is shown in Fig. C1. All joints share the same structure parameters ($\gamma_0 = 0$, $\beta_0 = \pi/4$, and $R_0 = 50$ mm) as well as the same dimensions for the leaf beams. The material for the leaf beams is stainless steel, with a Poisson's ratio of 0.3 and a Young's modulus of 200 GPa, while the remaining parts are assumed to be rigid.

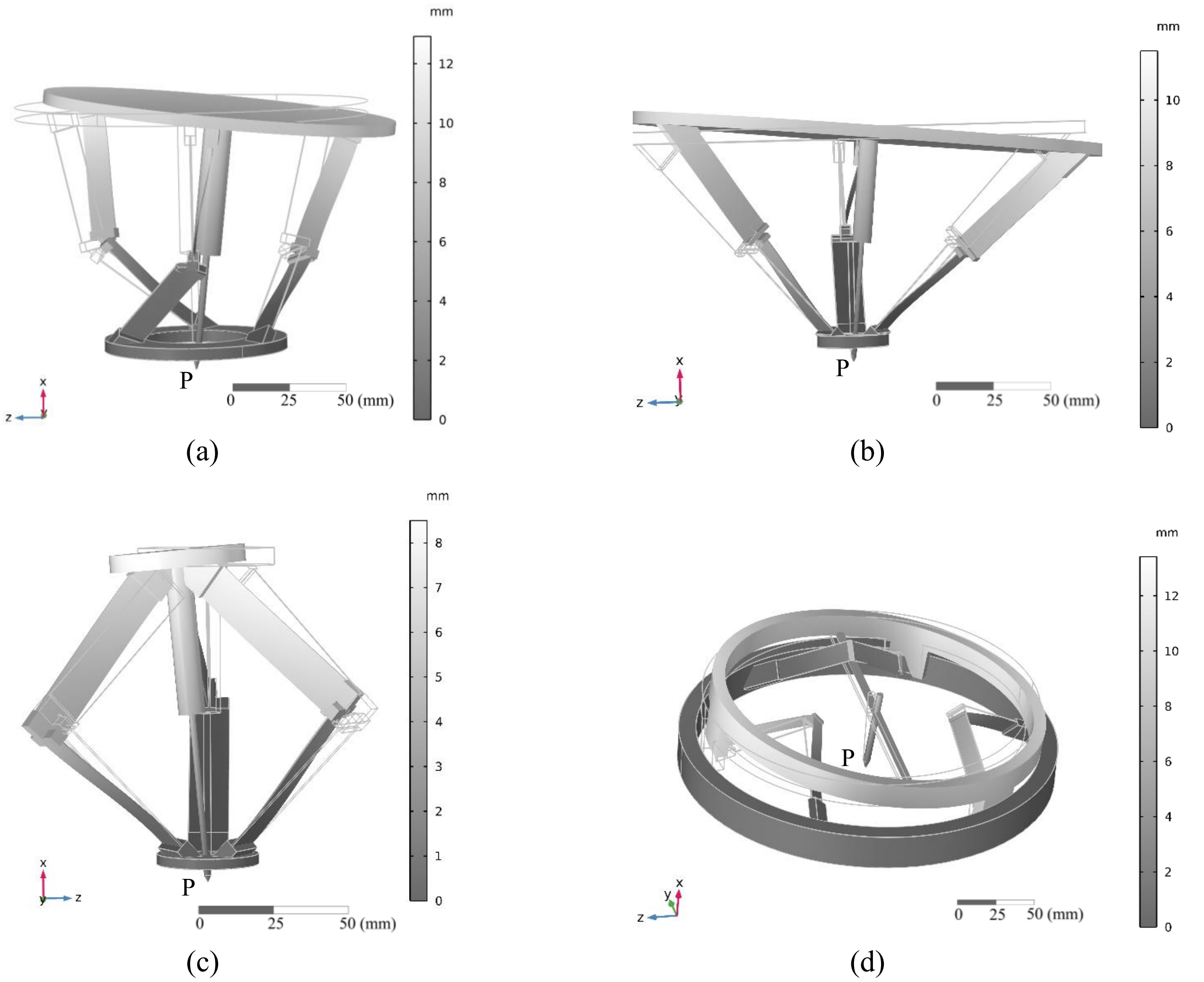

Figure C1 The deformed spherical joints under combined forces and moments (all obtained in FEA): (a) spherical joint with non-orthogonal leaf beams; (b) spherical joint with I-shape leaf beams; (c) spherical joint with L-shape leaf beams; (d) spherical joint with folded leaf beams.

Table Caption list

Table 1 Geometry parameters of four representative configurations derived from the GSTC leaf beam 9

Table 2 Maximum centre drift comparison (γ_0 ranging from 0 to 2π and R_0 equals to 50 mm)..........27

Table 3 The geometry parameters of the spherical joint with L-shape leaf beams.............................28

Figure Caption list

Figure 1 Compliant mechanisms with equivalent single-translation constraints: (a) wire beam with constraint line along the beam axial direction (length direction); (b) I-shape leaf beam [7]; (c) GSTC leaf beam. 6

Figure 2 Four representative configurations in comparison: (a) I-shape leaf beam ($\beta_{xi} = \pi/2$; $\beta_{yi} = 0$; $\beta_{zi} = 0$); (b) non-orthogonal leaf beam ($\beta_{xi} = \pi/2$; $\beta_{yi} = \pi/6$; $\beta_{zi} = \pi/6$); (c) L-shape leaf beam ($\beta_{xi} = \pi/2$; $\beta_{yi} = 0$; $\beta_{zi} = \pi/2$); (d) folded leaf beam ($\beta_{xi} = \pi/2$; $\beta_{yi} = \pi/2$; $\beta_{zi} = \pi/2$). 9

Figure 3 (Colour lines) The displacement comparison between the FEA and analytical results for the non-orthogonal leaf beam, subjected to incremental forces in the Y-direction, a constant force in the X-direction and a constant moment along the X-direction: (a) the resultant displacement X_{si} ; (b) the resultant displacement Y_{si} ; (c) the resultant displacement Z_{si} ; (d) the resultant rotation θ_{xsi} ; (e) the resultant rotation θ_{ysi} ; (f) the resultant rotation θ_{zsi} ;...11

Figure 4 (Colour lines) The displacement comparison between the FEA and analytical results for the I-shape leaf beam, subjected to incremental forces in the Y-direction, a constant force in the X-direction and a constant moment along the X-direction: (a) the resultant displacement X_{si} ; (b) the resultant displacement Y_{si} ; (c) the resultant displacement Z_{si} ; (d) the resultant rotation θ_{xsi} ; (e) the resultant rotation θ_{ysi} ; (f) the resultant rotation θ_{zsi} ; 11

Figure 5 (Colour lines) The displacement comparison between the FEA and analytical results for the L-shape leaf beam, subjected to incremental forces in the Y-direction, a constant force in the X-direction, and a constant moment along the X-direction: (a) the resultant displacement X_{si} ; (b) the resultant displacement Y_{si} ; (c) the resultant displacement Z_{si} ; (d) the resultant rotation θ_{xsi} ; (e) the resultant rotation θ_{ysi} ; (f) the resultant rotation θ_{zsi} ; 12

Figure 6 (Colour lines) The displacement comparison between the FEA and analytical results for the folded leaf beam, subjected to incremental forces in the Y-direction, a constant force in the X-direction and a constant moment along the X-direction: (a) the resultant displacement X_{si} ; (b) the resultant displacement Y_{si} ; (c) the resultant displacement Z_{si} ; (d) the resultant rotation θ_{xsi} ; (e) the resultant rotation θ_{ysi} ; (f) the resultant rotation θ_{zsi} ; 12

Figure 7 Spherical joints: (a) wire beam based spherical joint; (b) spherical joint using non-orthogonal leaf beams; (c) spherical joint using I-shape leaf beams; (d) spherical joint using folded leaf beams; (e) spherical joint using L-shape leaf beams. A video showcasing the design of the general spherical joint is available on YouTube: https://youtu.be/tWx_8c3q-Qw. 13

Figure 8 General spherical joint with GSTC leaf beams: (a) geometry labeling; (b) top view of the coordinate systems. 15

Figure 9 (Colour lines) The displacement comparison between the FEA and analytical results for the spherical joint with non-orthogonal leaf beams, subjected to incremental moment along the Y-direction, a constant moment along the X-direction and a constant force in the Z-direction: (a) the resultant displacement X_t ; (b) the resultant displacement Y_t ; (c) the resultant displacement Z_t ; (d) the resultant rotation θ_{xt} ; (e) the resultant rotation θ_{yt} ; (f) the resultant rotation θ_{zt} ; 19

Figure 10 (Colour lines) The displacement comparison between the FEA and analytical results for the spherical joint with I-shape leaf beams, subjected to incremental moment along the Y-direction, a constant moment along the X-direction and a constant force in the X-direction: (a) the resultant displacement X_t ; (b) the resultant displacement Y_t ; (c) the resultant displacement Z_t ; (d) the resultant rotation θ_{xt} ; (e) the resultant rotation θ_{yt} ; (f) the resultant rotation θ_{zt} ; 19

Figure 11 (Colour lines) The displacement comparison between the FEA and analytical results for the spherical joint with L-shape leaf beams, subjected to incremental moment along the Y-direction, a constant moment along the X-direction and a constant force in the X-direction: (a) the resultant displacement X_t ; (b) the resultant displacement Y_t ; (c) the resultant displacement Z_t ; (d) the resultant rotation θ_{xt} ; (e) the resultant rotation θ_{yt} ; (f) the resultant rotation θ_{zt} ; 20

Figure 12 (Colour lines) The displacement comparison between the FEA and analytical results for the spherical joint with folded leaf beams, subjected to incremental moment along the Y-direction, a constant moment along the X-direction and a constant force in the X-direction: (a) the resultant displacement X_t ; (b) the resultant displacement Y_t ; (c) the resultant displacement Z_t ; (d) the resultant rotation θ_{xt} ; (e) the resultant rotation θ_{yt} ; (f) the resultant rotation θ_{zt} ; 20

Figure 13 (Colour lines) The centre drift comparison between the FEA and analytical results for the spherical joint with non-orthogonal leaf beams, subjected to incremental moment along the Y-direction, a constant moment along the X-direction and a constant force in the X-direction: (a) the resultant displacement D_{xc}; (b) the resultant displacement D_{yc}; (c) the resultant displacement D_{zc}; 21

Figure 14 (Colour lines) The centre drift comparison between the FEA and analytical results for the spherical joint with I-shape leaf beams, subjected to incremental moment along the Y-direction, a constant moment along the X-direction and a constant force in the X-direction: (a) the resultant displacement D_{xc}; (b) the resultant displacement D_{yc}; (c) the resultant displacement D_{zc}; 22

Figure 15 (Colour lines) The centre drift comparison between the FEA and analytical results for the spherical joint with L-shape leaf beams, subjected to incremental moment along the Y-direction, a constant moment along the X-direction and a constant force in the X-direction: (a) the resultant displacement D_{xc}; (b) the resultant displacement D_{yc}; (c) the resultant displacement D_{zc}; 22

Figure 16 (Colour lines) The centre drift comparison between the FEA and analytical results for the spherical joint with folded leaf beams, subjected to incremental moment along the Y-direction, a constant moment along the X-direction and a constant force in the X-direction: (a) the resultant displacement D_{xc}; (b) the resultant displacement D_{yc}; (c) the resultant displacement D_{zc}. 23

Figure 17 (Colour lines) The influence of geometry parameters γ_0, β_0, and R_0 on the center drift of the spherical joint with non-orthogonal leaf beams under constant motion stage rotation (θ_{xt} = 0.2 rad, θ_{yt} = 0.3 rad and θ_{zt} = 0.5 rad): (a), (b), and (c) illustrate the incremental changes in γ_0 and β_0 with a constant R_0 value of 50 mm; (d), (e), and (f) showcase the incremental changes in γ_0 and R_0 with a constant β_0 value of π/4;..24

Figure 18 (Colour lines) The influence of geometry parameters γ_0, β_0, and R_0 on the center drift of the spherical joint with I-shape leaf beams under constant motion stage rotation (θ_{xt} = 0.2 rad, θ_{yt} = 0.3 rad and θ_{zt} = 0.5 rad): (a), (b), and (c) illustrate the incremental changes in γ_0 and β_0 with a constant R_0 value of 50 mm; (d), (e), and (f) showcase the incremental changes in γ_0 and R_0 with a constant β_0 value of π/4; 25

Figure 19 (Colour lines) The influence of geometry parameters γ_0, β_0, and R_0 on the center drift of the spherical joint with L-shape leaf beams under constant motion stage rotation (θ_{xt} = 0.2 rad, θ_{yt} = 0.3 rad and θ_{zt} = 0.5 rad): (a), (b), and (c) illustrate the incremental changes in γ_0 and β_0 with a constant R_0 value of 50 mm; (d), (e), and (f) showcase the incremental changes in γ_0 and R_0 with a constant β_0 value of π/4; 26

Figure 20 (Colour lines) The influence of geometry parameters γ_0, β_0, and R_0 on the center drift of the spherical joint with folded leaf beams under constant motion stage rotation (θ_{xt} = 0.2 rad, θ_{yt} = 0.3 rad and θ_{zt} = 0.5 rad): (a), (b), and (c) illustrate the incremental changes in γ_0 and β_0 with a constant R_0 value of 50 mm; (d), (e), and (f) showcase the incremental changes in γ_0 and R_0 with a constant β_0 value of π/4; 26

Figure 21 Experimental setup: (a) the spherical joint with L-shape leaf beams (pin tip is the remote centre P joint); (b) testing rig; (c) an overview of the experimental platform. 29

Figure 22 (Colour lines) Comparison of experimental, FEA, and analytical results: (a) force-displacement relationship of the motion stage; (b) centre drift analysis by comparing analytical and FEA results; (c) centre drift analysis by comparing analytical and experimental results. 31

Figure 23 Spherical joint with inverted single-translation constraint: (a) the sketch of the geometry; (b) the deformed configuration. 32

Figure 24 Spherical joint with 45-degree I-shape leaf beams: (a) the sketch of the geometry; (b) the deformed configuration. 33

Figure 25 Demonstration of the spherical joint in the application of minimally invasive surgery......34

Figure 26 Other prototypes: (a) the spherical joint with non-orthogonal leaf beams; (b) the spherical joint with L-shape leaf beams; (c) the spherical joint with folded-leaf beams. 35

Figure A1 Description of leaf beam 1 subjected to a general loading condition and its resulting displacements …………………………………………………………………………………...40

Figure C1 The deformed spherical joints under combined forces and moments (all obtained in FEA): (a) spherical joint with non-orthogonal leaf beams; (b) spherical joint with I-shape leaf beams; (c) spherical joint with L-shape leaf beams; (d) spherical joint with folded leaf beams…………… 44